

2019-01-1953 Published 10 Jun 2019



Analysis and Automated Detection of Ice Crystal Icing Conditions Using Geostationary Satellite Datasets and In Situ Ice Water Content Measurements

Kristopher Bedka NASA Langley Research Center

Christopher Yost Science Systems and Applications, Inc.

Louis Nguyen NASA Langley Research Center

J. Walter Strapp Met Analytics, Inc.

Thomas Ratvasky NASA John Glenn Research Center

Konstantin Khlopenkov, Benjamin Scarino, Rajendra Bhatt, Douglas Spangenberg, and Rabindra Palikonda Science Systems and Applications, Inc.

Citation: Bedka, K., Yost, C., Nguyen, L., Strapp, J.W. et al., "Analysis and Automated Detection of Ice Crystal Icing Conditions Using Geostationary Satellite Datasets and In Situ Ice Water Content Measurements," SAE Technical Paper 2019-01-1953, 2019, doi:10.4271/2019-01-1953.

Abstract

Recent studies have found that high mass concentrations of ice particles in regions of deep convective storms can adversely impact aircraft engine and air probe (e.g. pitot tube and air temperature) performance. Radar reflectivity in these regions suggests that they are safe for aircraft penetration, yet high ice water content (HIWC) is still encountered. The aviation weather community seeks additional remote sensing methods for delineating where ice particle (or crystal) icing conditions are likely to occur, including products derived from geostationary (GEO) satellite imagery that is now available in near-real time at increasingly high spatio-temporal detail from the global GEO satellite constellation. A recent study using a large sample of co-located GEO satellite and in-situ isokinetic evaporator probe (IKP-2) total water content (TWC) datasets found that optically thick clouds with tops near to or above the tropopause in close

proximity (≤ 40 km) to convective updrafts were most likely to contain high TWC ($\text{TWC} \geq 1 \text{ g m}^{-3}$). These parameters are detected using automated algorithms and combined to generate a HIWC probability (PHIWC) product at the NASA Langley Research Center (LaRC). Seven NASA DC-8 aircraft flights were conducted in August 2018 over the Gulf of Mexico and the tropical Pacific Ocean during the HIWC Radar II field campaign. The convection sampled during four flights was observed by GOES-16 at 1- or 5-minute intervals, providing the first opportunity to analyze product performance from this new satellite. This paper will (1) present initial comparisons between GOES-16 and IKP-2 datasets during HIWC Radar II, (2) demonstrate GOES-16 products for select periods when high TWC was encountered with an emphasis on three flights with 1-minute imagery, (3) compare GOES observations and derived products from the HIWC Radar I and II campaigns.

Introduction

Geostationary (GEO) satellites routinely observe hazardous deep convective storms across the world. The term hazardous here refers to weather conditions such as lightning, flooding rainfall, damaging wind, hail, tornadoes, and aviation hazards such as turbulence and icing that are a threat to people, property, and/or transportation. Storms that produce these hazards exhibit a set of unique spatial, temporal, and multi-spectral patterns in GEO imagery. For example, convective clouds are extremely reflective and

opaque in visible wavelength imagery due to high concentrations of ice particles in their tops and a deep layer of hydrometeors below. Convective cloud tops are elevated to heights that can exceed 20 km above ground in especially intense storms. As the clouds rise, they become increasingly cold and the outflow from convective updrafts, commonly referred to as "anvil cloud", expands outward. Anvil temperatures typically fall somewhere between the convective equilibrium level and the tropopause. Strong atmospheric instability near the updraft and other in-storm dynamical processes provide energy that

enables cloud tops to penetrate through the anvil cloud. The height difference between the updraft cloud and anvil generates texture in satellite visible wavelength imagery and also a temperature contrast in infrared (IR) imagery. These anvil-penetrating updraft regions, commonly referred to as “overshooting tops”, appear colder than the anvil usually by at least 5 degrees Kelvin (K). When these strong convective updrafts penetrate through the anvil level, where the atmosphere is stable and resistant to vertical motions, gravity waves are generated that provide a visual indication of where strong ice mass flux away from the updraft is occurring. The waves also generate texture in visible imagery and occasionally temperature oscillations that are less prominent compared to texture and cold anomalies from overshooting top (OT) updrafts.

Convective updrafts rapidly transport high concentrations of ice particles into the anvil cloud layer. Recent studies have documented many events since the early 1990s where aircraft flight through deep convective storms and anvil cloud has resulted in jet engine power loss, loss of engine control, and/or engine damage [1, 2, 3]. [2] reported that engine events occurred in seemingly innocuous cloud regions with only light to moderate turbulence, infrequent lightning, and where the pilot’s radar indicated green or weaker echoes ($<$ approximately 30 dBZ), leading to their hypothesis that the aircraft were encountering high mass concentrations of small ice particles associated with convective updrafts, and ice accretion in the engine by ingested ice particles was likely the cause of the events. These encounters of high mass concentrations in low radar reflectivity have been termed high ice water content (HIWC) events. Icing of aircraft air data probes (e.g. air temperature sensors and pitot airspeed indicators) has also been recognized to occur in the same type of cloud conditions [1,2,4,5]. At the present time, there is no formal definition of HIWC based on in-situ ice water content. Many in the community choose $>$ 1.0 g m^{-3} as the HIWC threshold, but [5] found that air data probe anomalies can occur with ice water content $>$ 0.5 g m^{-3} averaged over a 10-minute period, and [43] found that 0.5 g m^{-3} could impact engine performance. Therefore, in this paper we refer to TWC measurements that exceed 0.5 g m^{-3} as “high TWC”.

Automated algorithms have recently been developed at NASA Langley Research Center (LaRC) to identify patterns in cloud tops associated with hazardous convection and ice particle icing conditions. A large and diverse database of in-situ total water content (TWC) observations has recently been collected by NASA and other international research aircraft during the European High Altitude Ice Crystal (HAIC) [6] and North American High Ice Water Content (HIWC) projects [8, 33]. These TWC observations paired with co-located products derived from GEO imagery showed that flight within or beneath clouds with cold temperatures relative to the tropopause, and high visible reflectance (or “optical depth”) that were in close proximity to textured gravity waves or overshooting tops (OTs) was most likely to encounter high TWC conditions [9]. Detections of these conditions were combined to generate an HIWC probability (PHIWC) product that was proven useful for discrimination of clouds with high TWC [9]. Other satellite-based algorithms for detection of HIWC conditions have also been developed that use a different combination of satellite-derived inputs and methods for combining these inputs to estimate HIWC likelihood [10, 11].

A new set of NOAA Geostationary Operational Environmental Satellites (GOES) have recently become operational, providing observations over much of the Western Hemisphere with four times better spatial detail than previous GOES satellites [22]. These GOES-16 and -17 satellites also observe two \sim 1000x1000 km “Mesoscale Domain Sectors” at 1-minute intervals and can observe a region up to every 30 seconds when these Sectors are aligned. Automated NASA LaRC HIWC detections applied to GOES-14 1-minute “super rapid scan” imagery collected during the 2015 NASA HIWC Radar I field campaign [8] showed the best correlation with in-situ TWC observations to date from any satellite-derived product [9,11]. Previous satellite-based HIWC studies were based on imagery collected at 10- to 30-minute intervals by GOES-13, Meteosat Second Generation, or the Multifunction Transport Satellite-1R (MTSAT-1R), a sampling frequency that is often inadequate for resolving rapidly evolving storm processes responsible for generating HIWC.

NASA conducted the HIWC Radar II field campaign in August 2018 to collect in-situ measurements within deep convection to compare to data collected in previous HIWC flight campaigns and to test new algorithms that can be applied to onboard aircraft weather radar observations to detect HIWC regions [8,13]. These measurements can also be used to further develop and test GEO satellite-based HIWC detection methods. Seven NASA DC-8 aircraft flights were conducted from 2-20 August 2018. The first two flights were based in Fort Lauderdale, Florida and sampled scattered convection and MCSs in the Gulf of Mexico. As the campaign progressed, the environment over the western Atlantic and Gulf of Mexico regions became extremely unfavorable for significant deep convection, so campaign operations were moved to the NASA Armstrong Flight Research Center in Palmdale, CA where the DC-8 aircraft is based. The five remaining flights were devoted to sampling tropical cyclone Lane, from the time of first classification as Tropical Depression 14-E on 15 August through Category 3 and 4 hurricane status on 20 August. Detailed descriptions of the campaign and corresponding aircraft radar-based HIWC research are provided by [8,13]

Storms sampled by three HIWC Radar II flights were observed via GOES-16 at 1-minute intervals through a request to NOAA from the campaign Forecast Team. Another flight was observed at 5-minute intervals. These data provide an excellent opportunity to analyze the performance of the LaRC PHIWC product as well as to continue to study cloud evolution coincident with HIWC that was depicted by satellite imagery and products. As Hurricane Lane moved westward on 18-20 August, GOES-16 observed it at an extremely oblique angle, so we used data from GOES-15 which observes with coarser spatial and temporal resolution. This paper will present GOES-16 analyses and demonstrations of the PHIWC product compared with co-located DC-8 in-situ datasets with a focus on the three flights with 1-minute imagery. A summary of the co-located satellite and aircraft observations from the other four flights is provided in the Appendix. GOES and in-situ TWC data aggregated across the entire HIWC Radar II campaign will also be shown and compared with data from the 2015 NASA HIWC Radar I campaign.

Data and Methods

GOES Satellite Observations and Derived Products

GOES Satellite Observations The GOES-15 and -16 satellites observed convective clouds sampled by the DC-8 during HIWC Radar II. The GOES-16 satellite, positioned at the equator and 75.2° West longitude, carries two meteorological instruments, the Advanced Baseline Imager (ABI, [12]) and Geostationary Lightning Mapper (GLM, [14, 15]). The ABI provides 0.5 km spatial resolution at nadir in the 0.63 μm visible channel and 2.0 km resolution in the 10.3 μm infrared channel, data from which were used in near real-time for HIWC Radar II flight planning and to generate the products featured in this paper. Satellite pixel sizes enlarge with increasing distance from the subsatellite point, reaching as large as 4.5 km for the IR channels during the 16 August 2018 Tropical Storm Lane flight. The ABI data for all flights were resampled to a fixed grid with a spacing of 0.5 km and 2.0 km for the visible and IR channels using methods described by [16]. This is done to ease spatial analysis methods that depend on distance calculations, such as the distance to the nearest OT or textured cloud pixel that are used to calculate PHIWC. A fixed grid also makes it easier to co-locate DC-8 data with the satellite products.

The ABI collects data every 5 minutes over a contiguous United States (CONUS) domain that covered the Gulf of Mexico and every 15 minutes outside of the CONUS domain. The ABI also has the capability to collect data every minute in two “Mesoscale Domain Sectors” (MDS) which each cover approximately 1000x1000 km regions. Upon request from the NASA HIWC team, NOAA devoted an MDS for most of the time when the DC-8 was flying through convection on 6 August (1200-1459 UTC), and the entire time spent sampling Lane on 15 and 16 August.

The GLM continuously observes radiances from lightning that are processed to identify lightning source regions. The sources are processed further to identify lightning “groups” which are essentially clusters of lightning-induced cloud illuminations. Further processing clusters groups into “flashes” which map organized channels of illuminations that humans are accustomed to seeing within convection. Further details and references about the GLM instrument and data processing can be found in [14,15]. Based on community experience with these new GLM products, it was determined that a combination of lightning products provided the best real-time guidance for avoiding persistent lightning-producing updraft regions. Though the research community has discovered some issues with GLM products [15], GLM data has been found useful for monitoring trends in convection intensity and was used to supplement cloud-to-ground lightning detections from the Vaisala National Lightning Detection Network (NLDN) and the DC-8 aircraft Stormscope WX-1000E for the two Gulf of Mexico flights [8]. Flights into tropical cyclone Lane were outside of the GLM field of view.

The GOES-15 Imager, positioned over the equator and 135° West longitude in August 2018, provides data in similar

visible and IR wavelengths to those described above for the ABI but at four times coarser spatial resolution. Resampling to a 4 km resolution was done for GOES-15 imagery, as well as GOES-13 and GOES-14 described below. GOES-15 collected data every 30 minutes for the 18 and 20 August flights which was its nominal operational scan frequency over the central Pacific Ocean. Scans observed Lane at approximately 10 and 40 minutes after the hour. Upon request by the HIWC Radar II Forecasting Team, NOAA operated GOES-15 in “rapid scan mode” on 19 August to observe Lane. Rapid scanning occurred in a somewhat irregular pattern, providing data approximately every 10 minutes for most of an hour, then every 2.5 minutes from 52 minutes after the hour through the end of the hour, yielding a total of up to 8 images/hour from 1900-1959 UTC and 2200-2259 UTC. There was a break in rapid scanning from 2030-2130 UTC when only 30-minute observations were collected.

GOES-13 and GOES-14 imagery from the 10 flights during HIWC Radar I has been reprocessed using the methods described below to compare with results from HIWC Radar II. This reprocessing incorporates a new method for optical depth retrieval, use of the MERRA-2 reanalysis [17] instead of MERRA-1 [18], and various other improvements and bug fixes included in the software since the publication of [9, 16]. The spatial resolution of the visible and IR imagery from these satellites is the same as GOES-15, but the image frequency varied depending on the day of flight as described by [9].

Satellite-Based Deep Convective Cloud Top Detection and HIWC Probability Products

As noted above, previous research based on data from the 2014 and 2015 flight campaigns conducted within the HAIC-HIWC project and also by NASA and North American partners indicated that flight through cold, optically thick cloud in close proximity ($< \sim 40$ km) to OTs or gravity waves was most likely to experience high TWC. Automated methods to identify convective cloud tops with these properties have been developed at NASA LaRC and are described in detail by [16]. Cold clouds are identified by through differencing the GOES IR temperature from the MERRA-2 tropopause temperature, interpolated in time and space to the GOES IR pixels. We used the MERRA-2 “blended tropopause temperature” (MERRA-2 parameter “TROPT”) product [17]. Tropopause temperature is spatially smoothed to eliminate patterns in the IR-tropopause difference that would mirror MERRA grid boxes in localized areas where the tropopause temperature varies over short distances. It is known that deep convection can modify the local tropopause, so variations in tropopause in the MERRA reanalysis especially in data-poor oceanic regions or over developing countries with few upper air observations are not especially meaningful. For our purposes, the tropopause serves as a stable reference to normalize IR temperatures across regions, much more so than the convective equilibrium level which is highly dependent on boundary layer temperature and moisture that has greater uncertainty in numerical model re-analyses and forecasts. This enables the products to perform comparably well for storms over the mid-latitudes where warmer tropopause and IR temperatures are typically present with convection than over the tropics.

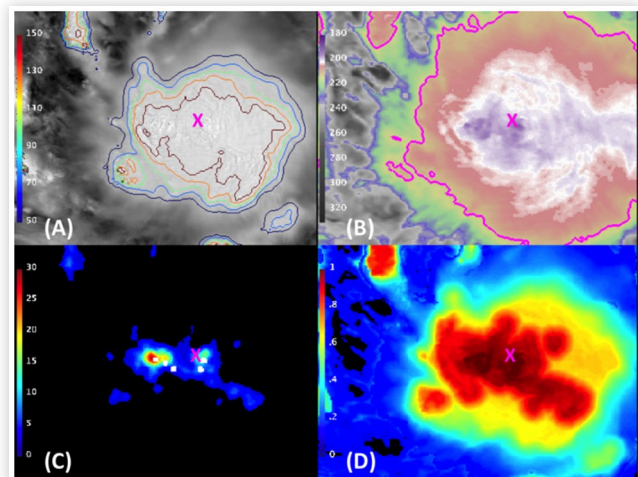
Anvil clouds and OTs are identified through spatial analysis of IR temperature patterns and IR - tropopause temperature differences. An OT probability is derived based on the IR-tropopause difference, the IR - regional anvil mean temperature difference, and metrics of anvil area and IR temperature spatial coherence. The highest OT probabilities are found for cloud tops near to or colder than the tropopause, cloud tops significantly colder (by 5+ K) than the regional mean (< ~50 km) anvil temperature, and within relatively large anvils. Pixels with OT probability ≥ 0.5 were combined with visible texture detections to derive a distance to the nearest OT or textured pixel product that is input to the PHIWC product.

The prominence of texture in visible imagery generated by OTs or gravity waves is quantified through spatial and Fourier analysis similar to the approach introduced by [16]. A number of improvements to the texture detection algorithm have been made in recent years including improved screening of false texture detections along anvil edges and also in complex scenes with anvils that generate shadows atop lower-level clouds below that can appear similar to OTs. Details of these improvements will be described in a future paper. The resulting visible texture rating product provides a similar range of values to [16], where gravity waves and weak OTs are assigned an integer rating less than 10, and more prominent OTs are assigned a larger rating that can exceed 50 for the most intense storms. An example of the texture rating product and the corresponding GOES-16 visible image is shown by Figure 1a and 1c, featuring two OT regions outlined by green shading in Figure 1c. We used a texture rating of 3 to identify OT and gravity wave regions. This is slightly lower than the value of 5 used by [9]. The lower rating provided greater continuity across images and a smoother animation which is desirable for end users of the product. Requiring a value of 5 can miss smaller or weaker OTs that could still generate high TWC.

Because the ABI has four times higher spatial resolution than GOES-13/14/15, OTs and gravity waves are more apparent/prominent and therefore generate a higher texture rating. GOES-16 ABI and the GOES-15 Imager best overlap along 105° West longitude and time-matched scans from these two satellites were used along this longitude band to develop a statistical correction to GOES-15 texture ratings to make them larger and as comparable as possible to ABI. These same corrections are also applied to GOES-13/14 given that they have identical visible channels as GOES-15.

Recent research using GOES-14 rapid scan imagery showed that texture rating is well correlated with the proximity of the 10 dBZ echo top, derived from NEXRAD multi-radar composites, to the tropopause. [19]. A higher echo top indicates a deeper, and in some cases stronger, updraft than a lower echo top. The relationship between texture and echo top makes physical sense, in that a “bumpier” cloud top in visible imagery indicates greater turbulence within the updraft and greater penetration of the cloud top above the anvil level that creates shadows and sharp contrasts in anvil reflectance. Another study using GOES-14 super rapid scan imagery found that higher texture ratings atop severe storms were correlated with stronger cloud top divergence derived using cloud-tracked atmospheric motion vectors, another proxy for a more intense updraft [20]. These studies give confidence that the

FIGURE 1 (A) GOES-16 visible image at 1927 UTC on 15 August 2018 during flight within Tropical Storm Lane. Cloud optical depth derived from visible reflectance is shown with colored contours, starting from an optical depth unit of 50 and increasing at 25 unit intervals. Clouds with optical depth > 50 had a mean TWC > 0.5 g m⁻³ based on IKP-2 data from 50 flights during the 2014 and 2015 HAIC and HIWC flight campaigns [9]. The NASA DC-8 was located at the position indicated by the magenta X. A maximum TWC of 2.16 g m⁻³ was observed by the IKP-2 less than a minute from the time of the image. (B) GOES-16 IR temperature for the same scene as panel (A). The magenta contour indicates regions where the IR temperature was within 15 K of the NASA MERRA-2 reanalysis tropopause temperature, a threshold where the mean TWC began to notably rise based on data from the 50 flights mentioned above. The only pixels colder than the tropopause are colored in dark purple near the X and directly to the west. (C) Texture detection rating from GOES visible imagery (color shading) and detections of anvil-penetrating updrafts or “overshooting tops” from GOES IR imagery (white dots). Greater visible texture (warm colors) indicates a greater above-anvil penetration by the updraft region cloud top. (D) The NASA LaRC PHIWC product.



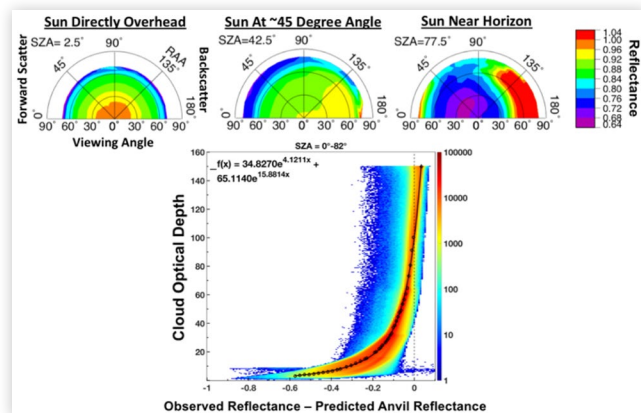
© 2019 SAE International; NASA Glenn Research Center.

texture detection algorithm is providing a representative proxy of updraft cloud height and storm intensity.

Cloud optical depth is derived using a new method based on the difference between a pixel's observed reflectance (normalized by the cosine(solar zenith angle)) and a climatological database of anvil cloud reflectance accumulated across the full range of possible solar zenith angle, satellite viewing zenith angle, and relative azimuth angle combinations. We refer to this database as the “predicted anvil reflectance”. The anvil reflectance database was derived using one-year of half-hourly GOES-13, GOES-15, and Himawari-8 satellite imagery. The premise behind this approach is that a cloud with reflectance near to or exceeding the predicted anvil reflectance based on climatology is extremely optically thick. Examples of this anvil reflectance climatology for overhead sun (solar zenith angle (SZA) < 5°), SZA of ~45°, and SZA > 70° are shown in Figure 2-top. One can see that anvil

© 2019 SAE International; NASA Glenn Research Center.

FIGURE 2 (top panels) The distribution of climatological anvil reflectance derived for varying solar zenith angle, viewing angle (x-axis), and relative azimuth angle ranging from 0-180°, where 0° indicates direct forward scattering and 180° indicates direct back scattering. (bottom) A statistical fit between optical depth derived from the CERES Cloud Subsystem and the difference between the satellite-observed reflectance and predicted anvil reflectance from climatology.



© 2019 SAE International; NASA Glenn Research Center.

reflectance varies significantly depending on how the cloud is illuminated and how the satellite views the cloud with respect to the position of the sun, especially when the sun is near to the horizon. This observed minus predicted reflectance was statistically related to optical depth from the Satellite Cloud and Radiation Property retrieval System (SatCORPS) which is based on cloud retrieval methods developed for MODIS within the NASA CERES Cloud Subsystem applied to GEO imagery [21]. The SatCORPS optical depth was used to derive PHIWC in [9]. This relation yielded an exponential function (Figure 2-bottom) that allows for immediate retrieval of optical depth with values analogous to what would be provided by SatCORPS, without having to wait for several minutes while SatCORPS processes imagery over large geographic domains. The GOES visible reflectance is spatially averaged prior to input into the exponential function, with a preference for the bright pixels in the 28 km averaging kernel, to minimize shadowing and localized dark spots that cause an artificially low bias in optical depth and a correspondingly lower PHIWC.

As can be seen in the bottom panel of Figure 2-bottom, a ~10% decrease in reflectance can lower optical depth from 150 to ~80, which would lower PHIWC. When many satellite visible wavelength detectors such as those from GOES are exposed to the space environment, their sensitivity degrades so satellites like GOES-13 that have been in space the longest would have sensed lower reflectance if this degradation were not accounted for. To address this, all GOES satellite imagers are matched in time and space with the MODIS sensor that has been designed to provide a stable visible channel signal throughout its lifetime. These satellite inter-calibration methods are based on those developed within the Global Satellite Inter-Calibration System (GSICS) group, some of which were initially developed at NASA LaRC [22]. After matching with MODIS, calibration uncertainty is estimated

to be ~1% which is the best that can be expected using these available datasets.

The study by [9] used comparable weighting of HIWC likelihood based on fuzzy logic membership functions derived using the IR-tropopause difference, distance to OT/texture, and cloud optical depth parameters to derive PHIWC. As briefly mentioned in [9], OTs and gravity waves can be quite variable over short periods of time, especially in disorganized convection. When products are generated from 1-minute imagery and animated, an OT present at one minute which then disappears for a couple minutes and later reappears will generate “flicker” in the PHIWC product. In addition, texture and cold spots associated with updrafts can be very subtle and sometimes not detectable, yet the cloud top is still very optically thick and cold and can contain HIWC. To account for this, the distance to the nearest OT/textured pixel field has been down-weighted to 0.15 and the weights for optical depth and tropopause-relative IR brightness temperature have been increased to 0.40 and 0.45, respectively, relative to the weights published in [9].

In this paper, we only analyze the characteristics of the LaRC PHIWC product derived from data that includes visible channel information, which of course would only be available during daytime. Visible data, which provides four times better spatial resolution than IR data, are extremely useful for identifying textured updraft regions linked to HIWC that may not produce a notable signal in IR imagery. [9] discusses differences in product performance with IR-only information, and additional perspectives on the topic are provided in the Discussion section of this paper.

An example of GOES-16 satellite imagery and derived products for a scene during the 15 August flight is shown in Figure 1. At this time, the DC-8 was at an altitude of ~36 kft (~12 km) which corresponded to an air temperature of -45° C, and its location is denoted by the magenta X symbol. The aircraft was ~4 km below cloud top estimated from the GOES IR temperature (Figure 6a). Five-second mean Total Water Content (TWC) estimates from the isokinetic TWC evaporator (IKP-2) [7,34,35] exceeding 1.0 g m^{-3} were continuously observed from ~19:26:30 to 19:28:00, peaking at 2.16 g m^{-3} at 19:26:51. It can be seen that the DC-8 was within extremely optically thick cloud with IR temperatures near to or colder than the tropopause, and in close proximity (< 10 km) to an OT. The PHIWC product combines the optical depth, tropopause-relative IR temperature, and proximity to updraft information, which results in very high values for clouds in the center of the scene, including at the DC-8 location. A detailed description of the 15 August flight is provided in the following section.

Co-Location Between Satellite Data and Total Water Content Observations

We used the methods described by [9] to co-locate GOES products and DC-8 datasets. We accumulate IKP-2 TWC data at 45-second intervals and compute the mean TWC during these periods for matching with the GOES data. GOES is matched with TWC over time windows that depend on the GOES scan frequency. For example, when GOES-15 observed Lane at 30-minute intervals, all TWC data within +/- 15-minutes of a GOES image were matched. For GOES-16 5-minute observations of

Gulf of Mexico storms on 2 August, and for the 1-hour period when GOES-16 operated in 5-minute mode on 6 August, all TWC within ± 2.5 minutes were matched. A match period of ± 30 seconds was used for GOES-16 and GOES-14 from HIWC Radar I while these satellites were in 1-minute super rapid scan mode. Over a 45-second period, the DC-8 travels a ~ 9 km distance assuming typical cruise speeds between 200–210 m s^{-1} . This distance is comparable to the size of 1 to 2 GOES IR satellite pixels over the DC-8 flight domains during HIWC Radar II. In addition, wobbles in GOES-13/14/15 navigation of one pixel are quite common so there is always some uncertainty in GOES pixel locations. Lastly, cloud top height retrieval is not perfect so there is also uncertainty with regards to parallax correction. Use of 45-second data in our analysis accounts for GOES pixel size and these issues. The maximum 5-second TWC shown by [8] was also recorded and will be referenced throughout the text. Graphics shown and animations referenced in the below section display the 45-second mean TWC.

GOES-16 viewed tropical cyclone Lane at nearly a 60° view angle, which would cause the deep convective cloud tops to be displaced by over 30 km from their true ground-relative locations due to parallax. The parallax correction is done using the cloud top height retrieved from matching GOES IR temperature with the MERRA-2 temperature and height profile to ensure the best-possible co-location between GOES and DC-8 data.

As discussed in [9], the goal of our research is to discriminate clouds with HIWC from those without at the satellite pixel scale. We define cloud as $\text{TWC} \geq 0.1 \text{ g m}^{-3}$. This definition differs significantly from the definition used by the NCAR ALPHA product summarized by [11], who consider any non-zero TWC to be cloud. We find that satellite pixels with $\text{TWC} < 0.1 \text{ g m}^{-3}$ are very optically thin, warm, and are rarely found anywhere near to updrafts, and therefore are extremely easy to discriminate from pixels associated with $\text{TWC} > 0.5 \text{ g m}^{-3}$ and especially $> 1.0 \text{ g m}^{-3}$. Including these very low TWC values in the cloudy pixel population significantly decreases HIWC detection algorithm false alarm rate and makes results inconsistent with those derived from the LaRC PHIWC product. We also consider $\text{TWC} \geq 0.5 \text{ g m}^{-3}$ as a threshold where TWC is notable, rather than a higher threshold of 1.0 g m^{-3} used by many in the community. In addition, distinguishing between clouds that contain 0.5 g m^{-3} versus 1.0 g m^{-3} is very challenging using satellite-derived products [9], whereas discriminating clouds with $\text{TWC} < 0.5 \text{ g m}^{-3}$ is more realistic.

GOES Analyses of HIWC Radar II Flights

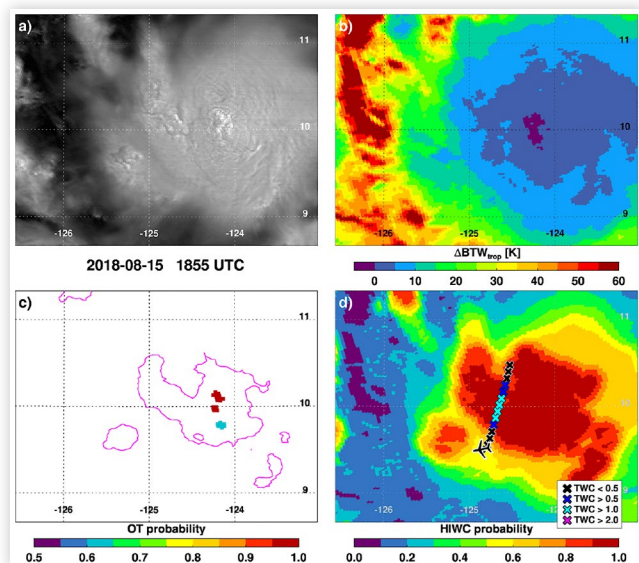
The following discussion will focus on the 15 August 2018 flight through Tropical Depression 14-E which later became Tropical Storm and Hurricane Lane. Selected GOES-16 examples from flights through cellular oceanic convection over the Gulf of Mexico on 16 August and the flight through Tropical Storm Lane on 16 August will also be shown, though

these days will not be discussed in as much detail as the 15 August flight. Co-locations between GOES-15 products and aircraft data for the 18–20 August flights are shown in the Appendix. Animated imagery in the same 4-panel format as shown below for all 2018 flights are available via the web links at [23, 24, 25, 26, 27, 28]. The graphics show a 10-minute history of TWC observations ending at the time of the GOES image being displayed. An aircraft icon indicates the position of the DC-8 at the time of the GOES image. Statistical relationships between GOES and TWC observations, aggregated across the entire HIWC Radar II field campaign will be also be presented. The relationship between PHIWC and TWC compiled across all HIWC Radar II flights will also be discussed and will be compared with results from HIWC Radar I.

15 August 2018

After a long transit flight from Palmdale, the DC-8 approached Tropical Depression 14-E at 1830 UTC, and subsequently completed a traverse through the cold and optically thick cloud shield of the storm system at 1855 UTC. IR temperatures within this cloud were typically 5–10 K warmer than the tropopause (blue shading, Figure 3b), with embedded areas colder

FIGURE 3 (a) GOES-16 visible image at 1855 UTC on 15 August 2018 during flight within Tropical Depression 14-E. (b) GOES-16 IR temperature - MERRA-2 tropopause temperature. Negative values (purple) indicate pixels colder than the tropopause. (c) Texture detection from GOES visible imagery (magenta) and OT probability generated from spatial patterns in GOES IR imagery and IR-tropopause temperature difference (colored dots). (d) The NASA LaRC PHIWC product overlaid with the flight track colorized to illustrate 45-second mean IKP-2 TWC values observed over the last 10 minutes to illustrate the time history of TWC in relation to current PHIWC patterns. The aircraft icon indicates the location of the DC-8 at the time of the image. The DC-8 altitude and static air temperature were 11 km and -45°C , respectively.



than the tropopause (purple). It is important to consider that tropopause-relative IR temperatures are shown with a color scale that varies in 5 K increments, so a change in color could mean that temperatures only varied by < 1 K. Along this traverse, 45-second mean TWC $> 0.5 \text{ g m}^{-3}$ was measured for several minutes, peaking with a 5-second mean of 1.9 g m^{-3} when in close proximity to an area of enhanced texture to the west of the aircraft track (Figure 3c). TWC $> 0.5 \text{ g m}^{-3}$, indicated by the blue flight track symbol, was regularly observed during flight through an area of PHIWC > 0.9 (Figure 3d). The aircraft returned to this region in the following minutes, passing approximately 10 km to the south of a prominent textured area colder than the tropopause, which triggered high IR-based OT probability (Figure 4). After a flight to the northeast into warmer cloud, the aircraft again traversed the cold cloud region, passing within 10 km of an OT located in the eastern half of the textured area (Figure 5, also highlighted above in Figure 1), and through the outflow to the southeast of another OT (orange dot, Figure 5c). The eastern OT (identified by red, yellow and blue dots in Figure 5c) persisted continuously throughout the duration of the flight and eventually became the center of circulation of Tropical Storm Lane. A pitot tube anomaly occurred during this flight segment which required that the aircraft exit cloud and descend to warmer temperatures to allow the pitot tube heater to melt the ice.

During the ~ 40 minute period while the pitot tube was being deiced and a new flight plan was developed, the storm became better organized in that the cold, textured cloud consolidated around the one primary OT region that became the center of circulation. Animated imagery suggests that the OT region was rotating and generated a very thin plume of cirrus above the primary anvil to the east of the OT ([25], Figure 18a). This above-anvil cirrus plume pattern indicates the presence of a strong tropopause-penetrating updraft that has been found to be highly correlated with severe weather in continental convection [30]. The plume in this case is not

FIGURE 4 Same as Figure 3 but at 1908 UTC. The DC-8 altitude and static air temperature were 11 km and -45° C , respectively.

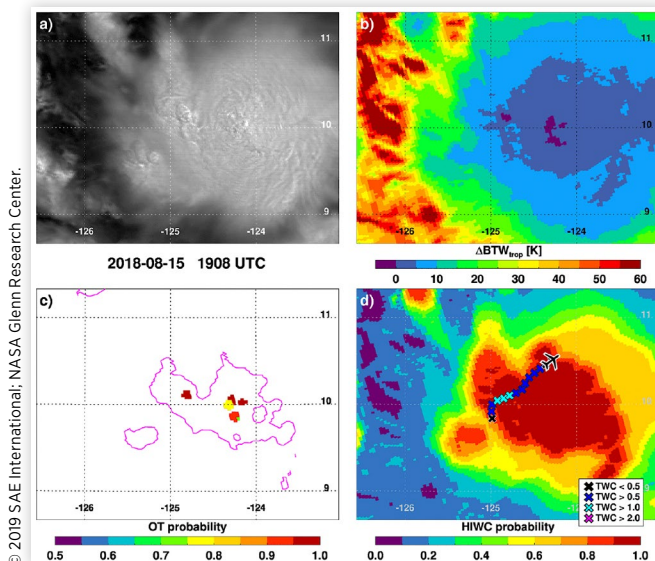
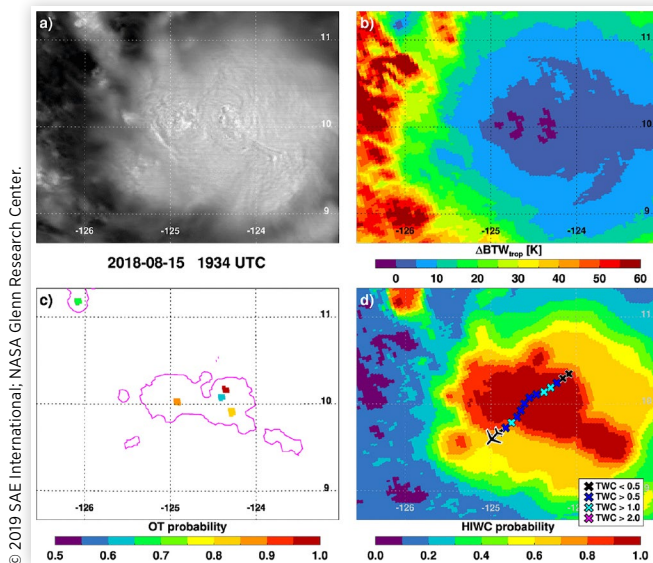


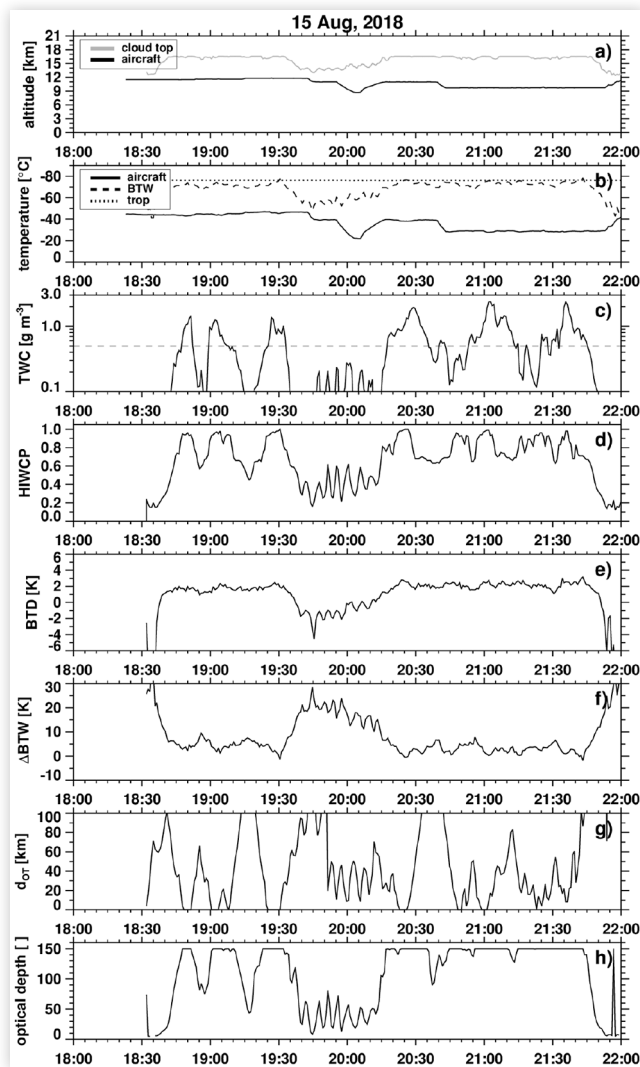
FIGURE 5 Same as Figure 3 but at 1934 UTC. The DC-8 altitude and static air temperature were 11.1 km and -46° C , respectively.



nearly as prominent as those found atop continental storms, an example of which is shown in Figure 17. The plume has smoother texture and is slightly warmer (~ 2 - 3 K) than the adjacent anvil cloud, which often resulted in slightly lower PHIWC on the eastern side of the storm despite the fact that fresh outflow from the OT was being preferentially directed to the east and south. Traverses around the storm center revealed that the TWC was much higher to the east and south of the OT than to the north and west. This is clearly illustrated in Figures 18-21 of the Appendix which show imagery at 10-minute intervals as the DC-8 circumnavigated the OT region at an altitude of 9.14 km and static air temperature of -29° C . The Forecast Team had recommended flight directly through the OT region in the hopes of measuring the highest TWCs, but onboard weather radar indicated red echoes at flight level and the Stormscope found frequent lightning, so the OT was considered unsafe to penetrate. 45-second mean TWC was $> 2.0 \text{ g m}^{-3}$ within 10 km directly to the south of the OT edge and $> 1.0 \text{ g m}^{-3}$ to the east, beneath the above-anvil plume. As the DC-8 turned westward and traversed north of the OT, TWC exceeded 0.5 g m^{-3} only in one 45-second period. Low TWC on the north side was also found in a previous traverse at 2053 UTC (not shown but depicted in the animation at [25]). TWC periodically exceeded 0.5 g m^{-3} on the west side before rapidly increasing to $> 2.0 \text{ g m}^{-3}$ on the south side, similar to the observation ~ 30 minutes earlier.

Co-located satellite-derived products and DC-8 observations throughout the duration of the flight are shown in Figure 6. One can see some similarities in trends between the TWC and PHIWC products but also areas of distinct differences. Aside from the time period from ~ 1935 to 2015 UTC when the pitot tube was being deiced, the DC-8 regularly flew beneath cloud tops that were 0-10 K warmer than the tropopause. IR temperature varied by < 5 K while sharp variations in TWC were observed. The water vapor minus IR temperature difference, a product that has been described in the

FIGURE 6 (a-b) DC-8 aircraft altitude and air temperature compared to that of the cloud top derived from GOES-16 IR observations (BTW, panel (a)) and the tropopause (panel (b)). (c) 45-second mean IKP-2 TWC data. (d) PHIWC. (e) GOES-16 6.2 micron WV - 10.3 micron IR BT difference. (f) Tropopause-relative IR brightness temperature. Negative values indicate clouds colder than the tropopause. (g) Distance to the nearest IR-based OT detection or textured pixel in the visible channel. (h) Cloud optical depth.



© 2019 SAE International; NASA Glenn Research Center.

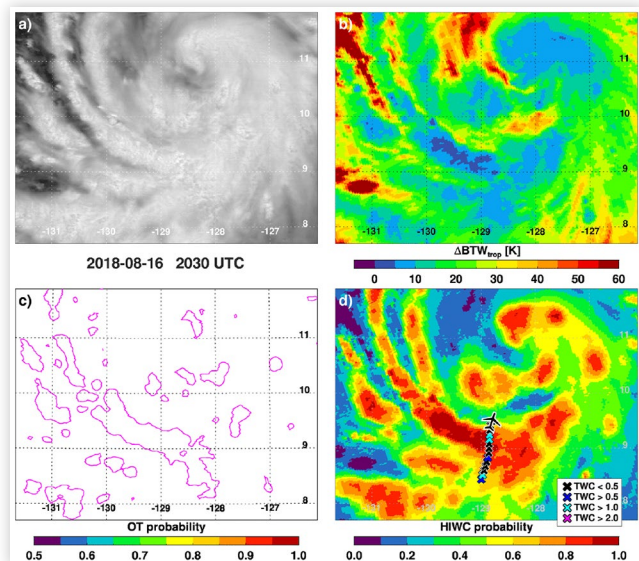
literature as being useful for anvil cloud and OT detection, shows even lower variability (1 K) than the IR-tropopause difference and therefore is not useful for discrimination of HIWC conditions, as was also found by [9]. The DC-8 generally stayed within the cold cloud shield of the storm system which was very reflective, yielding optical depths > 100. Such high optical depth generates maximum possible contribution to PHIWC based on [9]. Distance to the nearest textured cloud or IR-based OT detection provided the best agreement with TWC trends. Situations like Figures 18-21 demonstrate that the direction of outflow emanating from textured and/or OT cloud is also important to consider in addition to the distance from OT/textured cloud. The time periods from 2030-2045

UTC and 2105-2115 UTC (see Figure 19) when the DC-8 was far to the east of the OT region also demonstrate that high TWC can persist for relatively long distances (> 50 km) downstream of updraft regions if they are intense and persistent like in this storm. This may also be the case in long-lived continental MCSs and perhaps also supercell storms but no TWC observations have been collected in these storm types despite the findings of [3] which indicated that although in-service engine icing events occur predominantly in oceanic cloud, many have also occurred over land. An analysis of engine-events in continental clouds over South America and Africa has recently been provided by [36] to compare to the previous analysis of oceanic events over Southeast Asia [3]. Some differences in the location of events relative to the coldest IR regions of clouds are noted that are consistent with continental event clouds being more vigorous.

16 August 2018

After another long transit flight from Palmdale, the DC-8 reached Tropical Storm Lane around 1930 UTC. The cloud surrounding the center of Lane (near 11° N, 128° W) was initially quite cold with cloud top temperatures within 5 K of the tropopause, and well defined spiral banding to the southwest of the center. Throughout the ~3.5 hour period that the DC-8 sampled Lane, the cloud near Lane's center generally warmed, as is evident in the animation at [26] and in Figures 7-9. Some time was spent sampling this cloud but very few and generally brief encounters with high TWC occurred, so the focus shifted to the spiral band features south of the center. A north-south traverse through the spiral band with the greatest intensity was completed at 2030 UTC, and high TWC was observed (5-second peak TWC of 1.83 g m^{-3}) within an area of textured, cold, and optically thick cloud. Low TWC was found outside of the narrow core of the spiral band,

FIGURE 7 Same as Figure 3 but at 2030 UTC on 16 August during the DC-8 flight through Tropical Storm Lane at a 10.3 km altitude and -39° C static air temperature.



© 2019 SAE International; NASA Glenn Research Center.

FIGURE 8 Same as Figure 7 but at 2205 UTC. The DC-8 altitude and static air temperature were 9.2 km and -29°C , respectively.

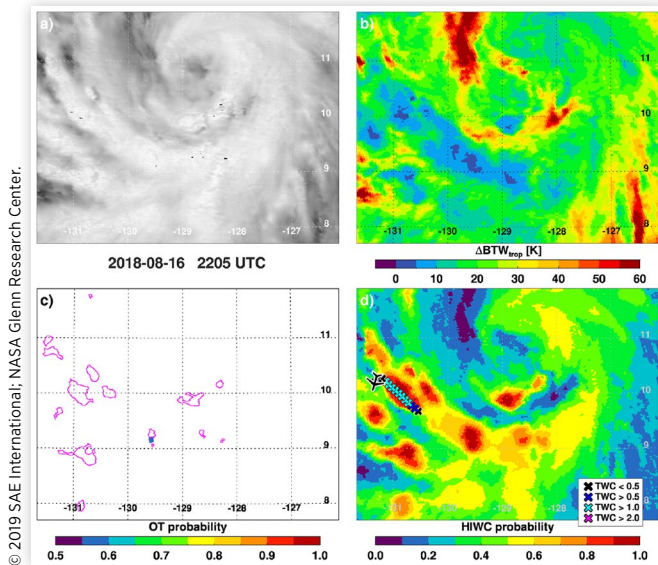
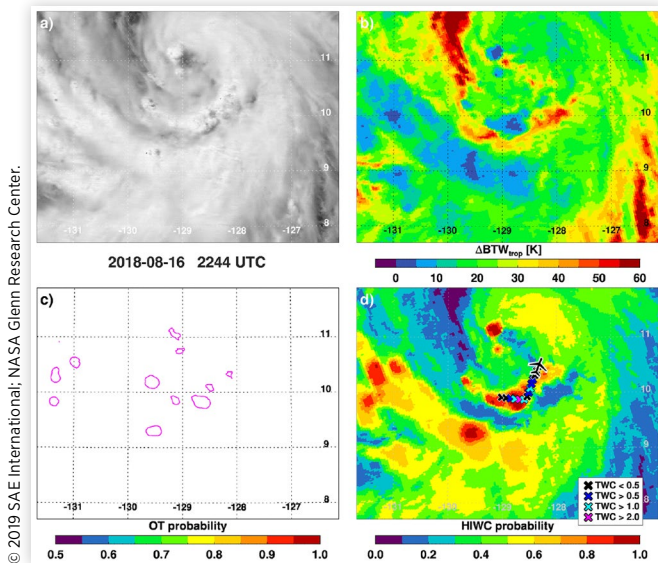
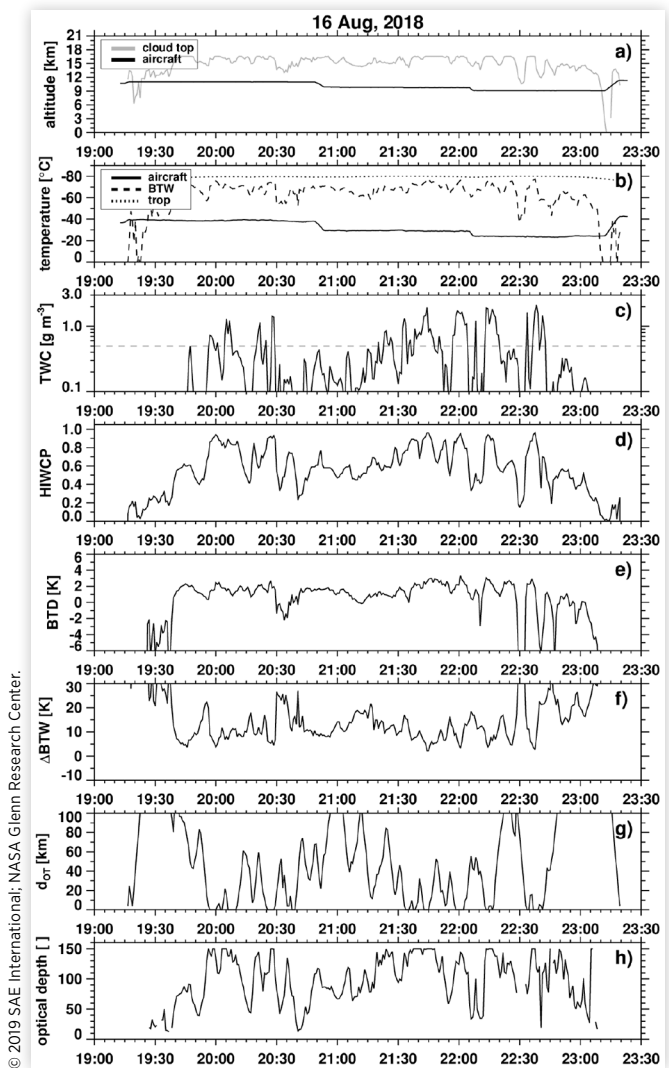


FIGURE 9 Same as Figure 7 but at 2244 UTC. The DC-8 altitude and static air temperature were 8.6 km and -24°C , respectively.



despite also being cold and optically thick, which generated high PHIWC that would be considered “false alarms” in this case. The southern spiral bands generally weakened throughout the flight. One particular band that was briefly sampled from north to south around 2030 UTC was sampled again from east to west as it re-intensified, beginning at 2130 UTC. An example of flight through this band that was completed at 2205 UTC is shown in Figure 8. A ~6-min long stretch of $\text{TWC} > 1.0\text{ g m}^{-3}$ was observed, peaking at 2.70 g m^{-3} , which was co-located with high PHIWC. About 40 minutes later as the DC-8 was on its way back to Palmdale, a new spiral band rapidly developed south of Lane’s center and was sampled

FIGURE 10 Same as Figure 6 but for the 16 August 2018 flight.



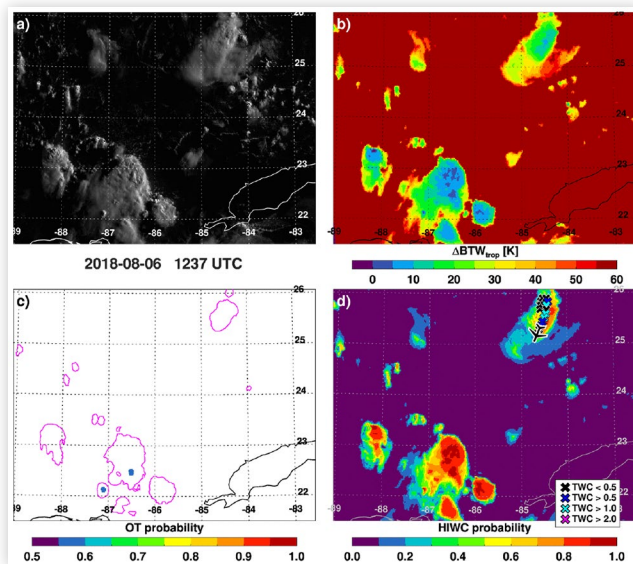
by the DC-8, during which a 45-second mean $\text{TWC} > 2.0\text{ g m}^{-3}$, peaking at 2.31 g m^{-3} , was observed.

Similar to the 15 August flight, co-located GOES and DC-8 data shows there is general agreement in trends between PHIWC and TWC. Encounters with HIWC were shorter lived given that narrow spiral bands were sampled most frequently during the flight. There was often very little variation in tropopause-relative IR temperature ($< 5\text{ K}$) as TWC increased from below to above 0.5 g m^{-3} . Distance to the nearest OT/textured pixel and optical depth showed more variation as high TWC was observed, further indicating that cold cloud tops can be fairly widespread but embedded updraft regions is where high TWC is most often located.

6 August 2018

The objective of this flight that originated from Fort Lauderdale was to sample fairly intense cellular convection in the Gulf of Mexico and near the northern edge of the Yucatan Peninsula. 1-minute super rapid scanning began at 1200 UTC, and in the

FIGURE 11 Same as Figure 3 but at 1237 UTC on 6 August during the DC-8 flight through cellular convection over the Gulf of Mexico. The DC-8 altitude and static air temperature were 9.7 km and -37°C , respectively.



10-minute window prior to 1237 UTC, the DC-8 sampled a storm cell with a textured, but much warmer cloud top than those sampled on 15 and 16 August (Figure 11). An OT had been present during this timeframe, but decayed by 1237 UTC. During the pass near that OT, the 45-second mean TWC exceeded 1.0 g m^{-3} in several instances, with the 5-second moving average TWC peaking at 2.86 g m^{-3} . Nearly 35 minutes later at 1311 UTC, the DC-8 sampled the storms that were pulsating in intensity near the Yucatan (Figure 12). A long stretch of $\text{TWC} > 1.0\text{ g m}^{-3}$ was found in an area of relatively high PHIWC, peaking at 1.34 g m^{-3} . This same cluster of convection was repeatedly sampled, and high TWC was periodically found generally in areas near cold textured/OT cloud tops (Figure 13).

FIGURE 12 Same as Figure 11 but at 1311 UTC.

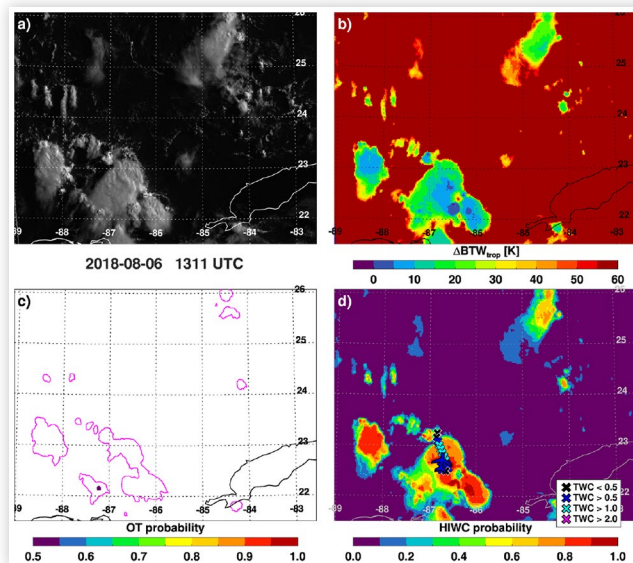
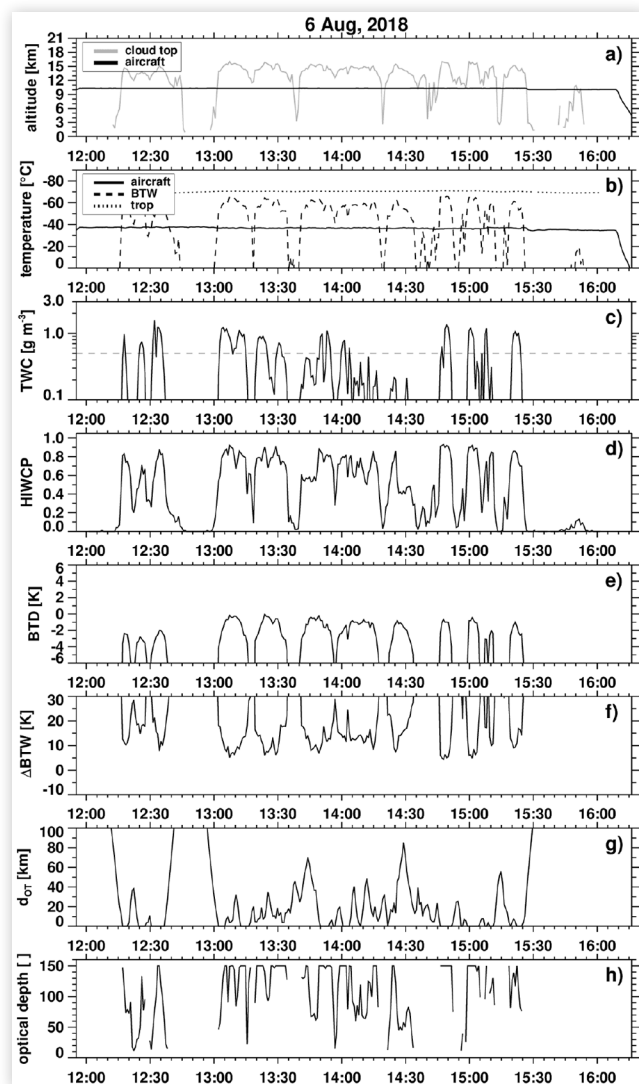


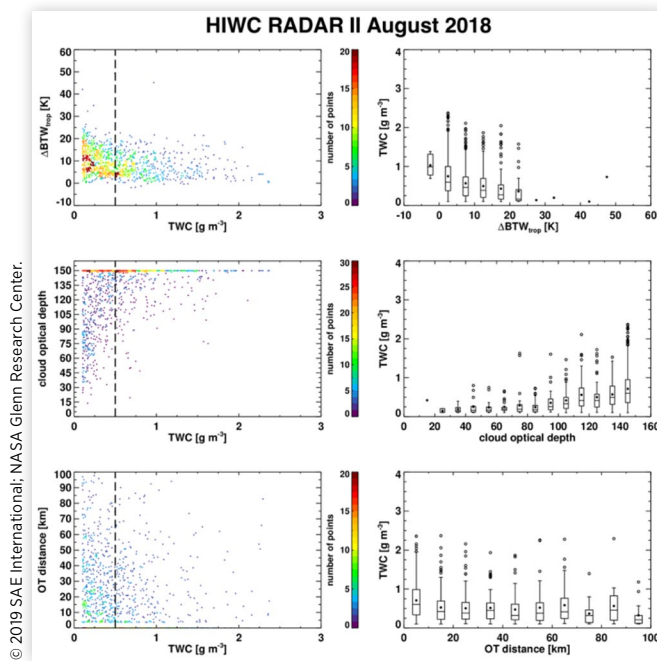
FIGURE 13 Same as Figure 6 but for the 6 August 2018 flight. Breaks in the optical depth indicate flight above water clouds or clear sky.



GOES Products Accumulated Throughout HIWC Radar I and II

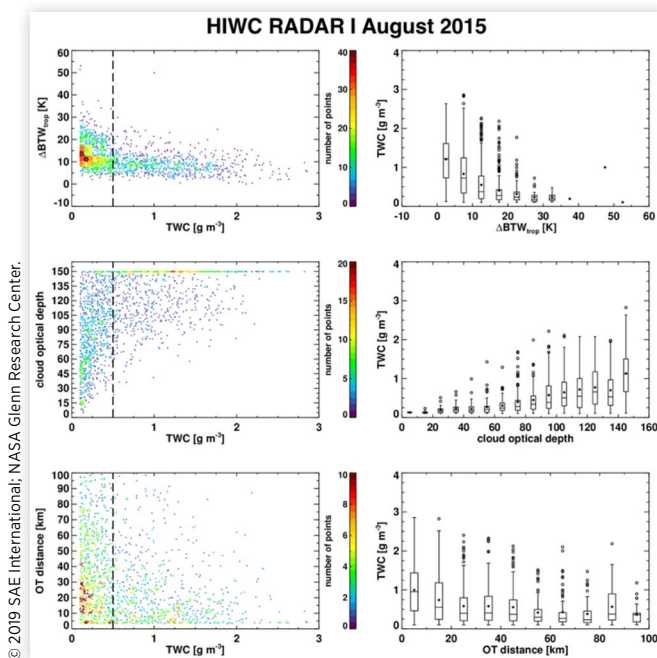
Figures 14 and 15 show the satellite inputs to the PHIWC product and 45-second mean TWC observations during HIWC Radar II and I, respectively. Convective clouds sampled by the DC-8 seldom had IR temperatures more than 30 K above the MERRA-2 tropopause temperature. Very few samples were collected in clouds colder than the tropopause. Though results presented above typically showed relatively little variability in tropopause-relative IR temperature as TWC increased from below to above 0.5 g m^{-3} , there was still a general increase in TWC as a function of IR temperature, consistent with the results of [9]. Optical depth also increased linearly with TWC beyond an optical depth of 80 (Figure 14, middle row). The whiskers in the TWC distribution also

FIGURE 14 (left panels) The distribution of satellite-derived parameter values as a function of 45-second mean TWC using all in-cloud data accumulated throughout HIWC Radar II. The color represents the density of points in a given region of the scatterplot. The vertical dashed line shows the 0.5 g m^{-3} threshold where satellite parameters start to lose sensitivity to TWC. (right panels) The distribution of TWC as a function of satellite-derived parameters. (top) IR-tropopause temperature difference ($\Delta\text{BTW}_{\text{trop}}$), (middle) cloud optical depth, (bottom) distance to the nearest OT/textured pixel.



© 2019 SAE International; NASA Glenn Research Center.

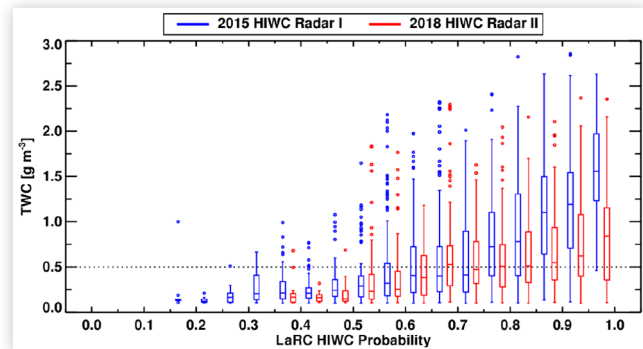
FIGURE 15 Same as Figure 14 but using data from HIWC Radar I.



© 2019 SAE International; NASA Glenn Research Center.

© 2019 SAE International; NASA Glenn Research Center.

FIGURE 16 The distribution of TWC as a function of PHIWC, binned at 0.05 intervals during HIWC Radar I (blue) and HIWC Radar II (red).



© 2019 SAE International; NASA Glenn Research Center.

increase within a distance of 40 km from an OT/texture, again consistent with [9], but the rate of TWC increase as the aircraft flew closer to these OT/texture pixels is not as large as [9]. The results from HIWC Radar II are generally consistent with HIWC Radar I, but one significant difference is that TWC was generally higher during Radar I. This demonstrates that convection sampled by the DC-8 in both campaigns generally had the same satellite-observed properties but the microphysical character of the convection was different. This could perhaps be related to the fact that the observations collected during HIWC Radar II were dominated by cyclone Lane with small contributions by cellular convection over the Gulf, whereas Radar I sampled several intense MCSs and that may have generated greater ice mass flux. Additional research is required to investigate this, which could also include examination of airborne radar observations and ambient winds to further characterize in-cloud microphysics, precipitation structures, and outflow rate.

The mean TWC begins to increase for $\text{PHIWC} \geq 0.6$ for both campaigns, with the difference again being that observed TWC was higher during HIWC Radar I (Figure 16). A steady increase in TWC as a function of PHIWC is expected if a HIWC detection product is performing well, as is the case here. $\text{TWC} \geq 0.5 \text{ g m}^{-3}$ was seldom observed when PHIWC was < 0.5 , suggesting that the probability could be rescaled to translate current values from 0.5 to 1.0 into a range of 0 to 1.0 which would provide greater dynamic range for the product and improved depiction of gradients associated with increases in TWC.

Discussion

The LaRC PHIWC product demonstrated the capability to pinpoint where within or below convective anvils that high TWC is most likely to be present. Detection methods for the aforementioned cloud properties linked to high TWC have recently been improved to enable PHIWC product generation over continental to hemispheric domains at full satellite spatial and temporal resolution in near-real time. The products are designed to operate with similar performance using data from any current or historical global GEO satellite. The

PHIWC product provides a diagnostic for where HIWC is currently present and could be used for short-term (up to 30 minute) strategic aviation decision making. Products are currently being evaluated in near-real time in the operational forecasting environment at several NOAA National Weather Service Center Weather Service Units. Additional evaluations by forecasters, researchers, and industry are welcomed.

A number of interesting findings and questions arise from this study. It was found that, in some cases like the 15 August 2018 flight, that the location of the aircraft with respect to the preferred direction of convective outflow may make a big difference with regards to the TWC values that are measured. Simply flying close to an OT region did not necessarily guarantee that high TWC would be observed. This was hypothesized by [9], and the results from the 15 August flights lends some credibility to that hypothesis.

During the 15 August flight, an above anvil cirrus plume was observed which slightly biased the GOES-16 IR temperature toward warmer values (by 2-3 K) and obscured textured gravity waves underneath the plume. The warmer IR temperature and reduced texture combined to reduce PHIWC where $TWC > 1.0 \text{ g m}^{-3}$ was repeatedly observed. Though the PHIWC was only reduced to values between 0.6 to 0.7 in this case, [Figure 17](#) shows that anvil warm anomalies due to plumes atop continental supercell storms can significantly impact a satellite-derived HIWC product. In this scene, a pair of supercells generated plumes over North Dakota. The western supercell had been producing a plume for nearly two hours and the plume extended for over 400 km. Baseball sized hail was reported from this storm 1.5 hours later. The severity of this storm at the time shown by [Figure 17](#) is unknown because that this region has low population density. The plume is quite smooth in contrast to the textured area around the western periphery of the OT. Texture is generated by the updraft turbulence, shadowing due to the sun being close to the horizon, and the interaction between the jet stream flow and the OT ([Figure 17a](#), magenta contour). The IR temperature within the plume was $\sim 5 \text{ K}$ warmer than the tropopause, and $\sim 12 \text{ K}$ warmer than the cloud slightly upwind of the OT. It is important to note that the OT is $\sim 5 \text{ K}$ warmer than the anvil cloud $\sim 10 \text{ km}$ to the west, which could be caused by mixing of the long-lived and tall OT with the warm stratospheric environment. The plume edge and other complex perturbations throughout the anvil generate reflectance enhancements that impact the optical depth. The PHIWC product indicates a broad area of high probability values consistent with high TWC during the flight campaigns described above, but also relatively low probability (0.5-0.6) within the plume.

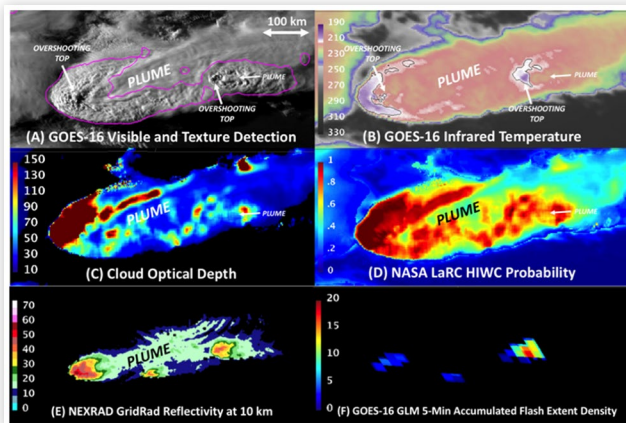
The NEXRAD GridRad horizontal reflectivity product shows strong reflectivity ($> 45 \text{ dBZ}$) at a 10-km altitude ([Figure 17e](#), [39,40]) for the two plume-producing updrafts, in addition to another core that does not appear particularly notable in the GOES imagery. Reflectivity $> 30 \text{ dBZ}$ extends over 30 km to the east of the western OT depicted by GOES and broad regions of $> 15 \text{ dBZ}$ echoes with small embedded regions of 20 dBZ are correlated with the plumes. We do not know if the plume area contains high TWC. Given that the plume was in the preferred direction of outflow from this extremely intense storm and precipitation echoes at flight level are displaced downstream and oriented along the axes of the plumes, it is

not unreasonable to assume high TWC would have been found somewhere within the plume. This is especially likely within a 30 km distance from westernmost cell where 30 dBZ echoes are located. Plumes are quite common atop severe storms across the US, so this case is not a rare exception. The research community needs to develop additional methods to diagnose the icing threat in these storm types, paired with in-situ observations to verify these methods. Automated above-anvil plume detection methods are currently under development at NASA LaRC and could help to address the low PHIWC bias near to convective cores if the detections were to be sufficiently accurate.

Another open question is related to the variability of TWC with altitude and how well would satellite products perform if compared against vertical profiles of TWC rather than single level in-situ measurements. [9] found that 82% of “false alarms” from the PHIWC product based on comparisons with in-situ data (i.e. high probability but $TWC < 0.5 \text{ g m}^{-3}$) had $TWC \geq 0.5 \text{ g m}^{-3}$ somewhere above or below the aircraft based on remote TWC estimated from the RADar SysTem Airborne (RASTA) cloud radar onboard the SAFIRE Falcon-20 during the HAIC-HIWC flight campaigns [38]. Comparisons with aircraft radar-estimated TWC from methods such as [13] could be useful for exploring TWC altitude dependence, which would offer additional benefits in that satellite-aircraft comparisons could be done over the much broader area observed by the radar rather than only along the flight track. Another point to consider is that TWC is referred to in this paper with absolute values, but given that TWC appears to decrease on average at colder temperatures [8], it may be better to refer to TWC in terms of percentile relative to the entire TWC observational database at a particular temperature level. With this approach, satellite-based algorithms would be validated based on percentiles rather than absolute TWC values. Such percentiles have already been prepared for the HAIC-HIWC and HIWC-RADAR I flight campaigns for an upcoming Aviation Rulemaking Advisory Committee (ARAC), and will be available shortly as an FAA Technical Report [37].

The animations and graphics featured in this paper show that while visible texture is quite common atop storms with high TWC, cold spots and OT signatures in IR imagery are not always easy to discern. This is a concern because only IR information is available at night when oceanic and continental MCSs likely to generate HIWC are quite common. [3] has shown that engine events occur at all times of the day and night. [9] showed that probability of detection of high TWC events decreases by 15% when IR-only inputs are used. Lightning observations are continuously collected by the Geostationary Lightning Mapper (GLM) instrument which could be aggregated in time to match the imaging frequency of ABI. GLM data at individual 20-second snapshots, the highest temporal resolution of GLM data distributed by NOAA, depicts lightning from convective cores as well as lightning that can propagate away from updrafts and through the anvil for long distances. Time aggregation of 8 km gridded lightning detections for periods of 1- to 5-minutes can allow one to easily discriminate convective cores where HIWC is found, which may not be especially notable in ABI imagery, from anvil lightning that is transient. [Figure 17f](#) shows an example of GLM lightning flash extent density [41, 42] accumulated over 5-minute period for the North Dakota storms

FIGURE 17 (A) GOES-16 visible imagery of a pair of severe supercell storms over North Dakota at 0030 UTC on 29 June 2018. The overshooting top updraft regions within the supercells are generating above-anvil cirrus plumes (see annotations), but the western storm plume is much longer lived and has a longer spatial extent than the eastern storm plume. Locations with LaRC visible texture rating ≥ 3 are outlined by the magenta contour. (B) GOES-16 IR temperature for the same scene. Locations where IR temperature is colder than the MERRA-2 tropopause are outlined by the black contour. (C) Cloud optical depth (D) PHIWC product, (E) Horizontal radar reflectivity factor at a 10 km altitude from the NEXRAD GridRad product (in dBZ). Only reflectivity ≥ 10 dBZ is shown. (F) The number of lightning flashes detected by GOES-16 GLM lightning from 0028-0032 UTC. This type of product is commonly referred to as “flash extent density”.



© 2019 SAE International; NASA Glenn Research Center.

discussed above. Similar to the NEXRAD GridRad product, three updraft cores are depicted, though the westernmost core with the highest NEXRAD reflectivity at 10 km is not producing as much lightning at this time as the easternmost core. The middle core would have been detected by visible texture, but it did not produce a notable IR temperature contrast with the anvil, so it was not detected as an OT. EUMETSAT will be launching their own geostationary Lightning Imager instrument in the coming years [32], which will provide continuous observations over the entire Western Hemisphere and parts of the Eastern Hemisphere at latitudes where lightning-producing convection typically occurs. GLM data is currently being tested in the PHIWC product in preparation for the widespread availability of space-borne lightning observations.

Summary

This paper summarizes GOES-based analyses of deep convective clouds sampled by the NASA DC-8 during the August 2018 HIWC Radar II flight campaign, and comparisons with results from the August 2015 HIWC Radar I campaign. This study is the first to demonstrate use of GOES-16 for HIWC research, and builds upon pioneering work by the authors that demonstrate the utility of 1-min super rapid scanning for analysis of satellite-observed cloud properties

in conjunction with in-situ TWC data. The characteristics of the GOES data and PHIWC product were generally consistent with analyses from previous campaigns, in that flight through cold, optically thick cloud in close proximity to updraft regions inferred from visible and IR patterns was most likely to experience high TWC. Examples and animations cited in this paper show that the PHIWC product captured TWC gradients quite well, especially when 1-minute imagery was available. As the DC-8 entered into regions with a PHIWC > 0.7 , TWC often increased and then later decreased as the aircraft left the high probability regions. Satellite-aircraft co-locations throughout the duration of flights show that most high TWC events are captured by high PHIWC, even for flights observed at 30-minute intervals on 18 and 20 August. The microphysical characteristics of convection sampled during HIWC Radar II were different than Radar I, in that similar satellite observed properties were observed in both campaigns, but the TWC was higher on average during Radar I. The mean TWC generally increased on average with increasing PHIWC, as would be expected from a useful product.

In some cases, low TWC ($< 0.5 \text{ g m}^{-3}$) was observed during high PHIWC occurrences. In addition, the 15 August flight demonstrated that the spatial distribution of high TWC can be skewed by outflow patterns. This highlights a significant limitation associated with use of geostationary imagery for HIWC detection, namely that patterns within cloud tops generally indicative of HIWC do not always match in-cloud microphysics and dynamics that generate the high TWC. We expect greater discrepancy between PHIWC and TWC during night when visible texture and optical depth is unavailable, but this could be mitigated to some extent through incorporation of ground- or space-based lightning data, or 3-D radar volumes such as those from NEXRAD GridRad.

Future Work

- Analyze DC-8 airborne weather radar reflectivity, radar-derived HIWC inferences [13], and GOES products to study the time evolution of HIWC-producing convection and to expand the spatial domain for validation of the GOES-based products beyond just the DC-8 flight track.
- Continue to analyze the satellite-observed properties of storms that cause air data probe anomalies.
- Combine geostationary lightning detection data with HIWC indicators derived from visible and IR imagery to improve the day-night consistency of the PHIWC product
- Develop a better understanding for the mechanisms behind spatial and temporal variability of anvil IR temperature using visible imagery, precipitation echo top height derived from weather radars, airborne- or space-based lidar, and/or convection-permitting numerical model simulations [39]
- Develop a better understanding of the microphysical differences between convection sampled during the HIWC Radar I and II campaigns

References

1. Lawson, R.P., Angus, L.J., and Heymsfield, A.J., "Cloud Particle Measurements in Thunderstorm Anvils and Possible Weather Threat to Aviation," *J. Aircraft* 35:113-121, 1998.
2. Mason, J.G., Strapp, J.W., and Chow, P., "The Ice Particle Threat to Engines in Flight," in *44th AIAA Aerospace Sciences Meeting*, Reno, Nevada, 9-12 Jan. 2006, abstract number AIAA 2006-206, 2006.
3. Bravin, M., Strapp, J.W., and Mason, J., "An Investigation into Location and Convective Lifecycle Trends in an Ice Crystal Icing Engine Database," in *Proceedings of the 2015 SAE International Conference on Icing of Aircraft, Engines, and Structures*, 2015.
4. Duviver, E., "High Altitude Icing Environment," in *Intl. Air Safety and Climate Change Conf*, Cologne, Germany, 8-9 Sep. 2010, 2010, available from https://www.easa.europa.eu/conferences/iascc/doc/Workshop%201%20Presentations/Workshop1_DAY%202/1_Duvivier_EASA/IASCC_E%20Duvivier.pdf
5. Haggerty, J., Rugg, A., Ratvasky, T., Strapp, W. et al., "Characterization of High Ice Water Content Conditions that Impact Air Data System Performance," in *19th American Meteorological Society Conference on Aviation, Range, and Aerospace Meteorology*, 2019, available online at: https://ams.confex.com/ams/2019Annual/video gateway.cgi/id/50567?recordid=50567&uniqueid=Paper350460&entry_password=453434
6. Dezitter, F., Grandin, A., Brenguier, J.-L., Hervy, F. et al., "HAIC - High Altitude Ice Crystals," in *5th AIAA Atmospheric and Space Environments Conference*, American Institute of Aeronautics and Astronautics, 2013, <http://arc.aiaa.org/doi/abs/10.2514/6.2013-2674> (Accessed Feb. 9, 2015).
7. Strapp, J.W., Lillie, L.E., Ratvasky, T.P., Davison, C.R. et al., "Isokinetic TWC Evaporator Probe: Development of the IKP2 and Performance Testing for the HAIC-HIWC Darwin 2014 and Cayenne 2015 Field Campaigns," in *8th AIAA Atmospheric and Space Environments Conference*, AIAA Aviation, AIAA 2016-4059, 2016, doi:10.2514/6.2016-4059
8. Ratvasky, T., Strapp, W., Lillie, L., Proctor, F. et al., "Summary of the High Ice Water Content (HIWC) RADAR Flight Campaigns," in *Proceedings of the 2019 SAE International Conference on Icing of Aircraft, Engines, and Structures*, 2019.
9. Yost, C.R., Bedka, K.M., Minnis, P., Nguyen, L. et al., "2018: A Prototype Method for Diagnosing High Ice Water Content Probability using Satellite Imager Data," *Atmos. Meas. Tech.* 11:1615-1637, doi:10.5194/amt-11-1615-2018.
10. de Laat, A., Defer, E., Delanoë, J., Dezitter, F. et al., "Analysis of Geostationary Satellite Derived Cloud Parameters Associated with Environments with High Ice Water Content," *Atmos. Meas. Tech.* 1359-1371, 2017, doi:10.5194/amt-10-1359-2017.
11. Haggerty, J., Defer, E., De Laat, A., Bedka, K. et al., "Detecting Clouds Associated with Jet Engine Ice Crystal Icing," *Bull. Amer. Meteor. Soc.* 100:31-40, 2019, doi:10.1175/BAMS-D-17-0252.1.
12. Schmit, T.J., Griffith, P., Gunshor, M.M., Daniels, J.M. et al., "A Closer Look at the ABI on the GOES-R Series," *Bull. Amer. Meteor. Soc.* 98:681-698, 2017, doi:10.1175/BAMS-D-15-00230.1.
13. Harrah, S., Strickland, J., Hunt, P., Proctor, F. et al., "Radar Detection of High Concentrations of Ice Particles-Methodology and Preliminary Flight Test Results," in *Proceedings of the 2019 SAE International Conference on Icing of Aircraft, Engines, and Structures*, 2019.
14. Goodman, S.J., Blakeslee, R.J., Koshak, W.J., Mach, D. et al., "The GOES-R Geostationary Lightning Mapper (GLM)," *Atmospheric Research* 125-126:34-49, 2013.
15. Rudlosky, S.D., Goodman, S.J., Virts, K.S., and Bruning, E.C., "Initial Geostationary Lightning Mapper Observations," *Geophys. Res. Lett.* 46:1097-1104, 2019.
16. Bedka, K.M. and Khlopenkov, K., "A Probabilistic Multispectral Pattern Recognition Method for Detection of Overshooting Cloud Tops using Passive Satellite Imager Observations," *J. Appl. Meteor. And Climatol.* 55:1983-2005, 2016, doi:10.1175/JAMC-D-15-0249.1.
17. Gelaro, R. and Co-Authors, MERRA-2 Overview: The Modern-Era Retrospective Analysis for Research and Applications, Version 2 (MERRA-2), *J. Clim.*, 2017, doi:10.1175/JCLI-D-16-0758.1
18. Rienecker, M. et al., "MERRA: NASA's Modern-Era Retrospective Analysis for Research and Applications," *J. Climate* 24:3624-3648, 2011, doi:10.1175/JCLI-D-11-00015.1.
19. Sandmael, T., Homeyer, C.R., Bedka, K.M., Apke, J.M. et al., "Evaluating the Ability of Remote Sensing Observations to Identify Significantly Severe and Potentially Tornadoic Storms," *J. Appl. Meteor. and Climatol.*, 2019, Provisionally accepted.
20. Apke, J.M., Mecikalski, J.R., Bedka, K., McCaul, E.W. et al., "Relationships between Deep Convection Updraft Characteristics and Satellite-Based Super Rapid Scan Mesoscale Atmospheric Motion Vector-Derived Flow," *Mon. Wea. Rev.* 146:3461-3480, 2018, doi:10.1175/MWR-D-18-0119.1.
21. Minnis, P., Sun-Mack, S., Young, D.F., Heck, P.W. et al., "CERES Edition-2 Cloud Property Retrievals using TRMM VIRS and Terra and Aqua MODIS Data, Part I: Algorithms," *IEEE Trans. Geosci. Remote Sens.* 49:4374-4400, 2011.
22. Doelling, D., Haney, C., Bhatt, R., Scarino, B. et al., "Geostationary Visible Imager Calibration for the CERES SYN1deg Edition 4 Product," *Remote Sens* 10:288, 2018.
23. 2 Aug. 2018 GOES-16 Animation: https://satcorps.larc.nasa.gov/field-exp/hiwc/NASA_LaRC_HIWC_detection_animation_20180802.mp4
24. 6 Aug. 2018 GOES-16 Animation: https://satcorps.larc.nasa.gov/field-exp/hiwc/NASA_LaRC_HIWC_detection_animation_20180806.mp4
25. 15 Aug. 2018 GOES-16 Animation: https://satcorps.larc.nasa.gov/field-exp/hiwc/NASA_LaRC_HIWC_detection_animation_20180815.mp4
26. 16 Aug. 2018 GOES-16 Animation: https://satcorps.larc.nasa.gov/field-exp/hiwc/NASA_LaRC_HIWC_detection_animation_20180816.mp4
27. 18 Aug. 2018 GOES-15 Animation: https://satcorps.larc.nasa.gov/field-exp/hiwc/NASA_LaRC_HIWC_detection_animation_20180818.mp4

28. 19 Aug. 2018 GOES-15 Animation: https://satcorps.larc.nasa.gov/field-exp/hiwc/NASA_LaRC_HIWC_detection_animation_20180819.mp4
29. 20 Aug. 2018 GOES-15 Animation: https://satcorps.larc.nasa.gov/field-exp/hiwc/NASA_LaRC_HIWC_detection_animation_20180820.mp4
30. Bedka, K., Murillo, E.M., Homeyer, C.R., Scarino, B. et al., "The Above-Anvil Cirrus Plume: An Important Severe Weather Indicator in Visible and Infrared Satellite Imagery," *Wea. Forecasting* 33:1159-1181, 2018, doi:10.1175/WAF-D-18-0040.1.
31. Grzych, M., Tritz, T., Mason, J., Bravin, M. et al., "Studies of Cloud Characteristics Related to Jet Engine Ice Crystal Icing Utilizing Infrared Satellite Imagery," in *Proceedings of the 2015 SAE International Conference on Icing of Aircraft, Engines, and Structures*, 2015.
32. Aminou, D.M., Bezy, J.L., Bensi, P., Stuhlmann, R. et al., "Meteosat Third Generation: Preliminary Imagery and Sounding Mission Concepts and Performances," in *Proc. SPIE 10567, International Conference on Space Optics - ICSO 2006*, 2017, 1056706, doi:10.1117/12.2308182
33. Strapp, J.W., Isaac, G.A., Korolev, A., Ratvasky, T. et al., "The High Ice Water Content (HIWC) Study of Deep Convective Clouds: Science and Technical Plan," FAA Rep. DOT/FAA/TC-14/31, 2016, 105, available at <http://www.tc.faa.gov/its/worldpac/techrpt/tc14-31.pdf>.
34. Davison, C.R., MacLeod, J.D., Strapp, J.W., and Buttsworth, D.R., "Isokinetic Total Water Content Probe in a Naturally Aspirating Configuration: Initial Aerodynamic Design and Testing," in *46th AIAA Aerospace Sciences Meeting and Exhibit*, Reno, Nevada, AIAA-2008-0435, Jan. 10, 2008.
35. Davison, C.R., Strapp, J.W., Lilie, L., Ratvasky, T.P. et al., "Isokinetic TWC Evaporator Probe: Calculations and Systemic Error Analysis," in *8th AIAA Atmospheric and Space Environments Conference*, June 17, 2016, Washington, DC, AIAA-4060, 2016, doi:10.2514/6.2016-4060.
36. Bravin, M., Strapp, J.W., Grzych, M., and Clarkson, M., "A Continuing Investigation of Diurnal and Location Trends in an Ice Crystal Icing Engine Event Data Base," in *Proceedings of the 2019 SAE International Conference on Icing of Aircraft, Engines, and Structures*, 2019.
37. Strapp, J.W., Schwarzenboeck, A., Bedka, K., Bond, T. et al., "An Assessment of Cloud Total Water Content and Particle Size from Flight Test Campaign Measurements in High Ice Water Content, Mixed Phase/Ice Crystal Icing Conditions: Primary In-Situ Measurements," *DOT/FAA/TC-18/1*, In preparation, 2019.
38. Protat, A., Delanoë, J., Strapp, J.W., Fontaine, E. et al., "2015: The Measured Relationship between Ice Water Content and Cloud Radar Reflectivity in Tropical Convective Clouds," *J. Appl. Meteor. Climatol.* 55:1707-1729, 2016, doi:10.1175/jamc-d-15-0248.1.
39. Homeyer, C.R., McAuliffe, J.D., and Bedka, K.M., "On the Development of Above-Anvil Cirrus Plumes in Extratropical convection," *J. Atmos. Sci.* 74:1617-1633, 2017, doi:10.1175/JAS-D-16-0269.1.
40. NEXRAD GridRad Homepage: <http://www.gridrad.org>
41. Bruning, E.C. and MacGorman, D.R., "Theory and Observations of Controls on Lightning Flash Size Spectra," *J. Atmos. Sci.* 70:4012-4029, 2013, doi:10.1175/JAS-D-12-0289.1.
42. Bruning, E.C., Tillier, C.E., Edgington, S.F., Rudlosky, S.D. et al., "Meteorological Imagery for the Geostationary Lightning Mapper," *J. Geophys. Res.*, 2019, In Preparation.
43. EUROCAE Publication ER-15, Feasibility Study Weather Radar for Ice Crystals Detection, Mar. 6, 2018, also available as RTCA document AFS-1, revised Sep. 2017.

Contact Information

Kristopher Bedka

22 Langley Blvd, Mail Stop 420
Hampton, VA 23681. U.S.A.
kristopher.m.bedka@nasa.gov
Office Phone: 1-757-864-5798

Acknowledgments

This work was supported by the Advanced Air Transport Technology Project within the NASA Aeronautics Research Mission Directorate Advanced Air Vehicles Program. The authors would like to acknowledge the FAA Aviation Research Division, and the NASA Aviation Safety Program for their leadership and support. For the NASA DC-8, primary support was provided by the NASA Armstrong DC-8 crew, including Tim Moes and Ken Norlin, NASA DC-8 project managers. We acknowledge Steven Harrah, NASA Langley's radar principal investigator, for his leadership during the NASA HIWC Radar I and II campaigns. We thank the McIDAS Data Center at the University of Wisconsin Space Science and Engineering Center for providing the archived GEO satellite imagery used in this analysis. We thank Cameron Homeyer (University of Oklahoma) from providing NEXRAD GridRad data, and Eric Bruning (Texas Tech University) and Scott Rudlosky (NOAA NESDIS STAR) for providing GOES-16 Geostationary Lightning Mapper flash extent density data included in this paper.

Definitions/Abbreviations

ABI - Advanced Baseline Imager

AHI - Advanced Himawari Imager

ARAC - Aviation Rulemaking Advisory Committee

CONUS - Contiguous United States

FAA - U.S. Federal Aviation Administration

GEO - Geostationary

GLM - Geostationary Lightning Mapper

GOES - Geostationary Operational Environmental Satellite

GSICS - Global Satellite Inter-Calibration System

HAIC - High-Altitude Ice Crystals

HIWC - High Ice Water Content

IKP-2 - Isokinetic Evaporator Probe-2

IR - Infrared

LaRC - NASA Langley Research Center

MERRA - Modern Era Retrospective analysis for Research and Applications

MODIS - MODerate Resolution Imaging Spectroradiometer

MTSAT-1R - Multifunction Transport Satellite- 1 Replacement

NASA - National Aeronautics and Space Administration

OT - Overshooting cloud Top

PHIWC - High Ice Water Content Probability

RASTA - RADar SysTem Airborne

SatCORPS - Satellite CLOUD and Radiation Property retrieval System

SZA - Solar Zenith Angle

TWC - Total Water Content

Appendix

FIGURE 18 (a) GOES-16 visible image at 1855 UTC on 15 August 2018 during flight within Tropical Depression 14-E. Locations of the overshooting cloud top at the storm center and above-anvil cirrus plume are identified with text. (b) GOES-16 IR temperature - MERRA-2 tropopause temperature. Negative values (purple) indicate pixels colder than the tropopause. (c) Texture detection from GOES visible imagery (magenta) and OT probability generated from spatial patterns in GOES IR imagery and IR-tropopause temperature difference (colored dots). (d) The NASA LaRC PHIWC product overlaid with the flight track colorized to illustrate 45-second mean IKP-2 TWC values observed over the last 10 minutes to illustrate the time history of TWC in relation to current PHIWC patterns. The aircraft icon indicates the location of the DC-8 at the time of the image. The DC-8 altitude and static air temperature were 9.14 km and -29°C , respectively.

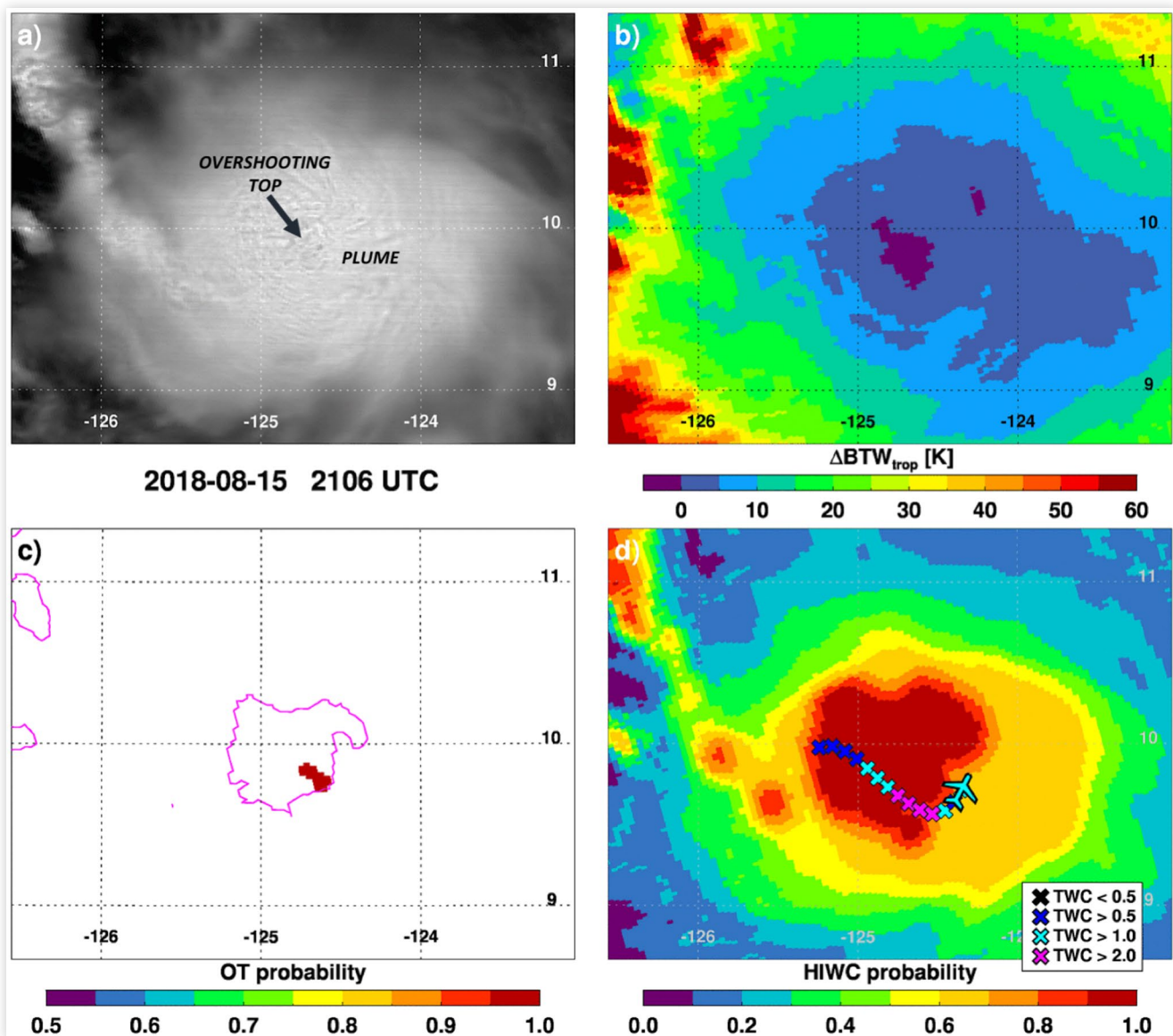


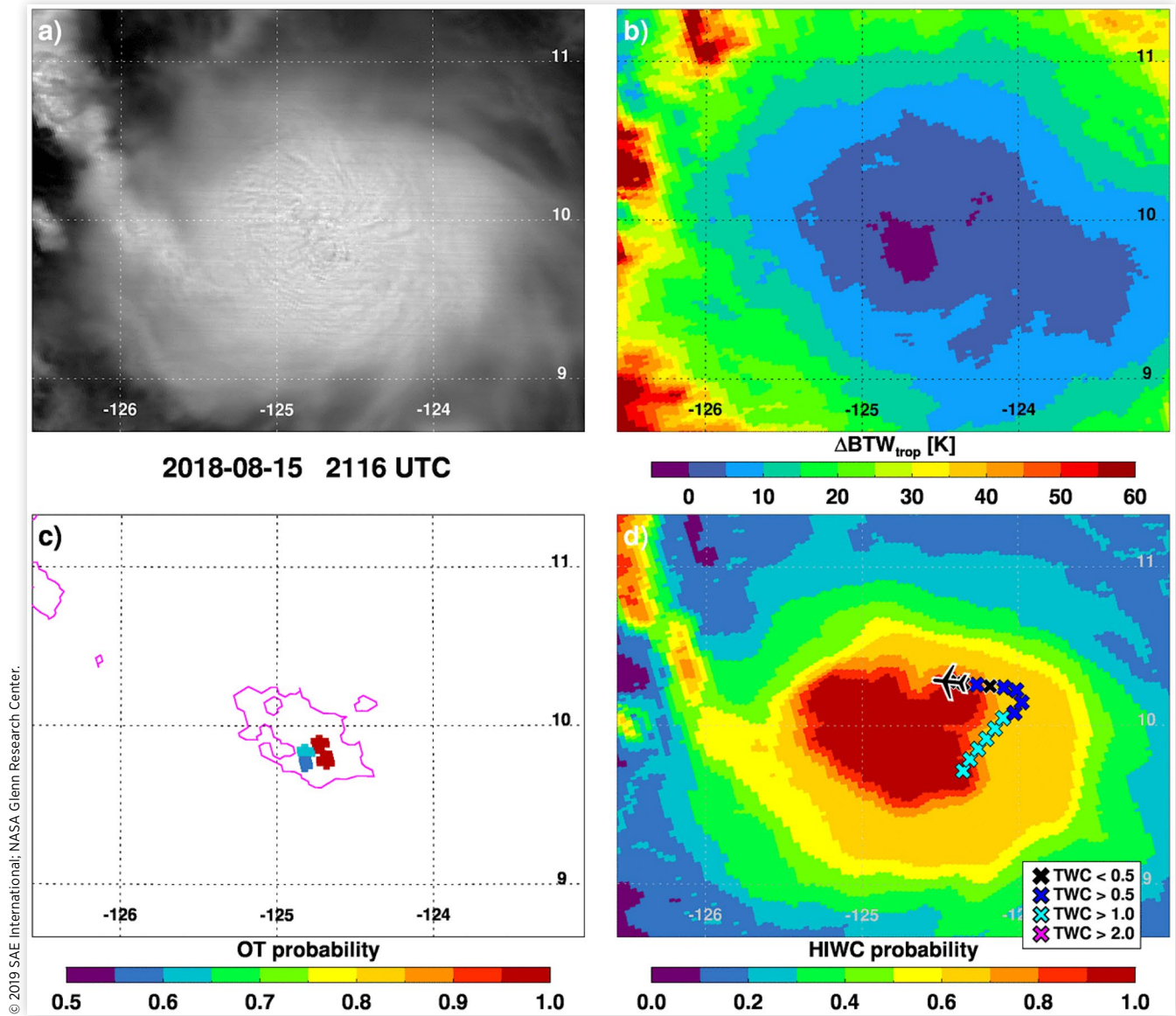
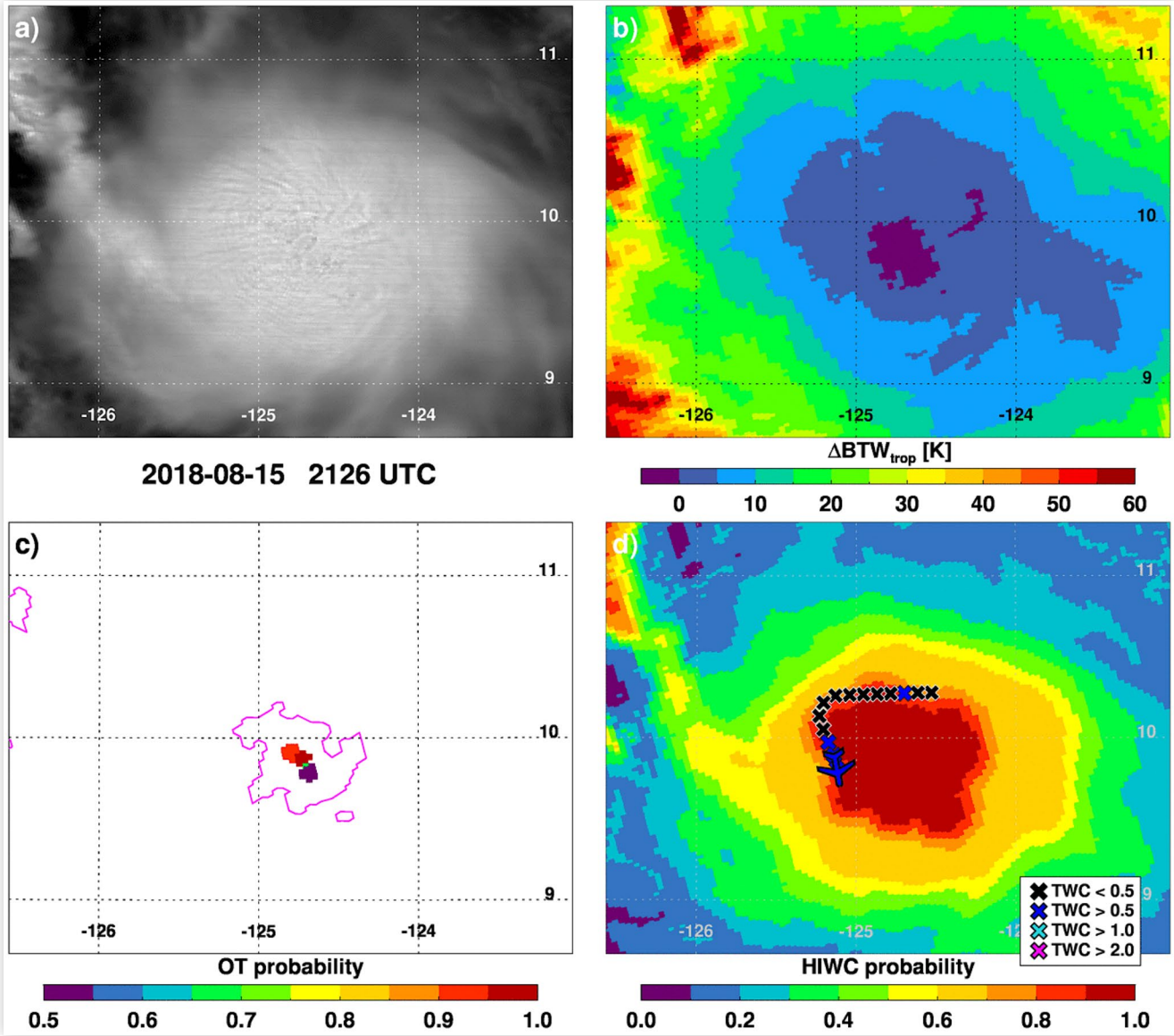
FIGURE 19 Same as Figure 18 but for 2116 UTC.

FIGURE 20 Same as Figure 18 but for 2126 UTC.



© 2019 SAE International; NASA Glenn Research Center.

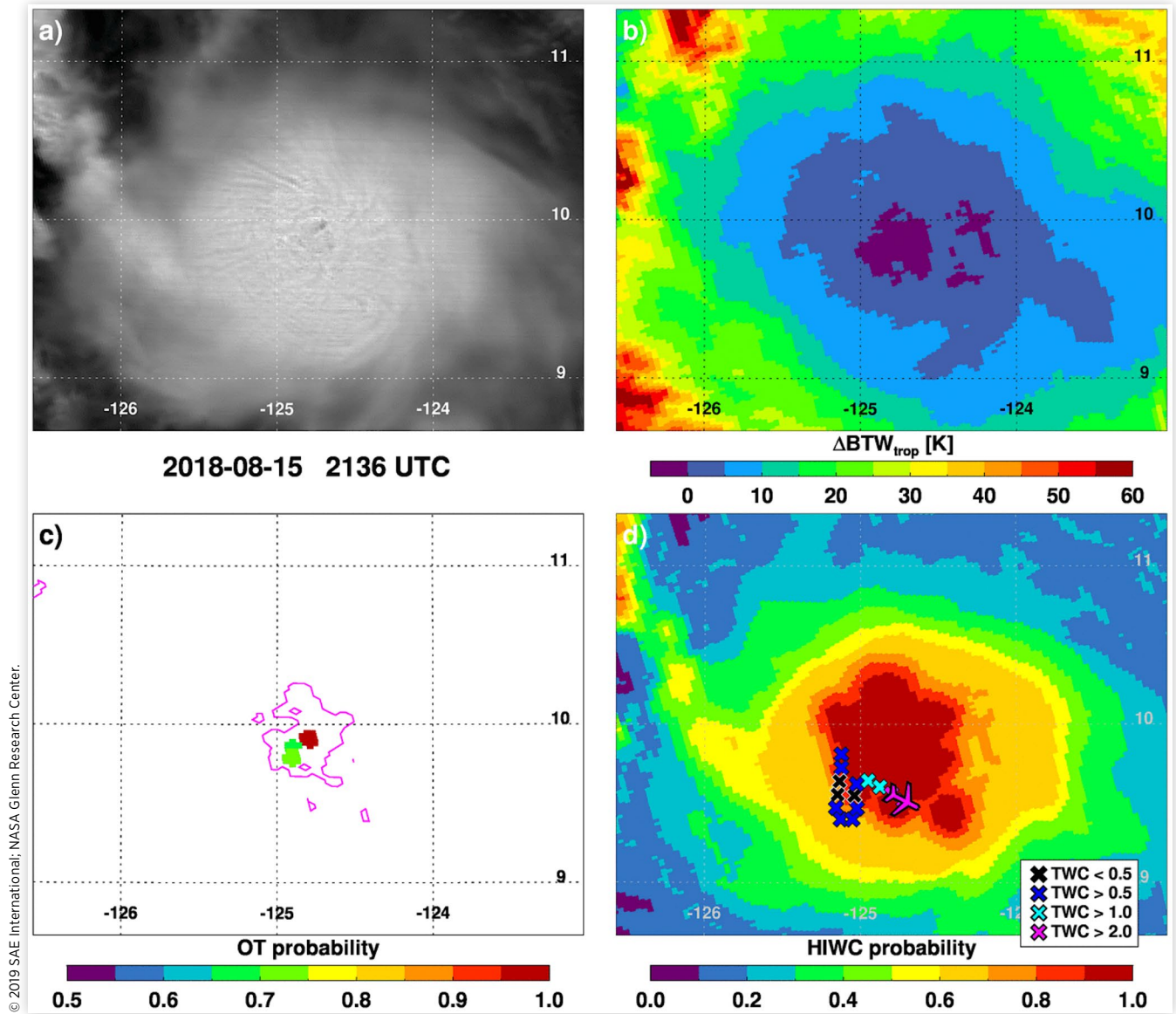
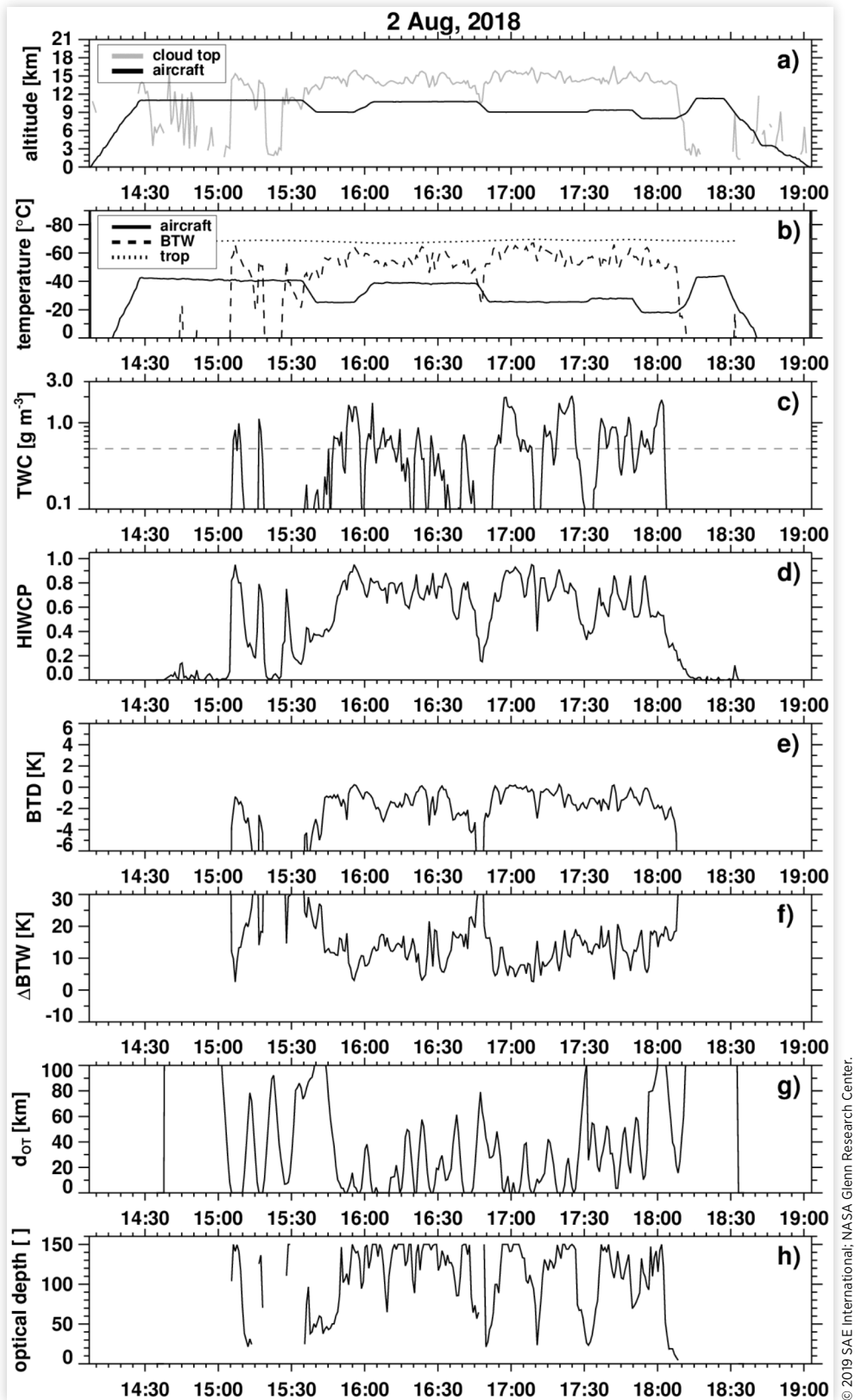
FIGURE 21 Same as Figure 18 but for 2136 UTC.

FIGURE 22 (a-b) DC-8 aircraft altitude and air temperature compared to that of the cloud top derived from GOES-16 IR observations (BTW) and the tropopause on 2 August 2018. The GOES-16 ABI observed these storms at 5-minute intervals. (c) 45-second mean IKP-2 TWC data. (d) PHIWC. (e) GOES-16 6.2 micron WV - 10.3 micron IR BT difference. (f) Tropopause-relative IR brightness temperature. Negative values indicate clouds colder than the tropopause. (g) Distance to the nearest IR-based OT detection or textured pixel in the visible channel. (h) Cloud optical depth.



© 2019 SAE International; NASA Glenn Research Center.

FIGURE 23 Same as Figure 22 but for GOES-15 data on 18 August 2018. The GOES-15 Imager observed these storms at 30-minute intervals, at approximately 10 and 40 minutes after the hour.

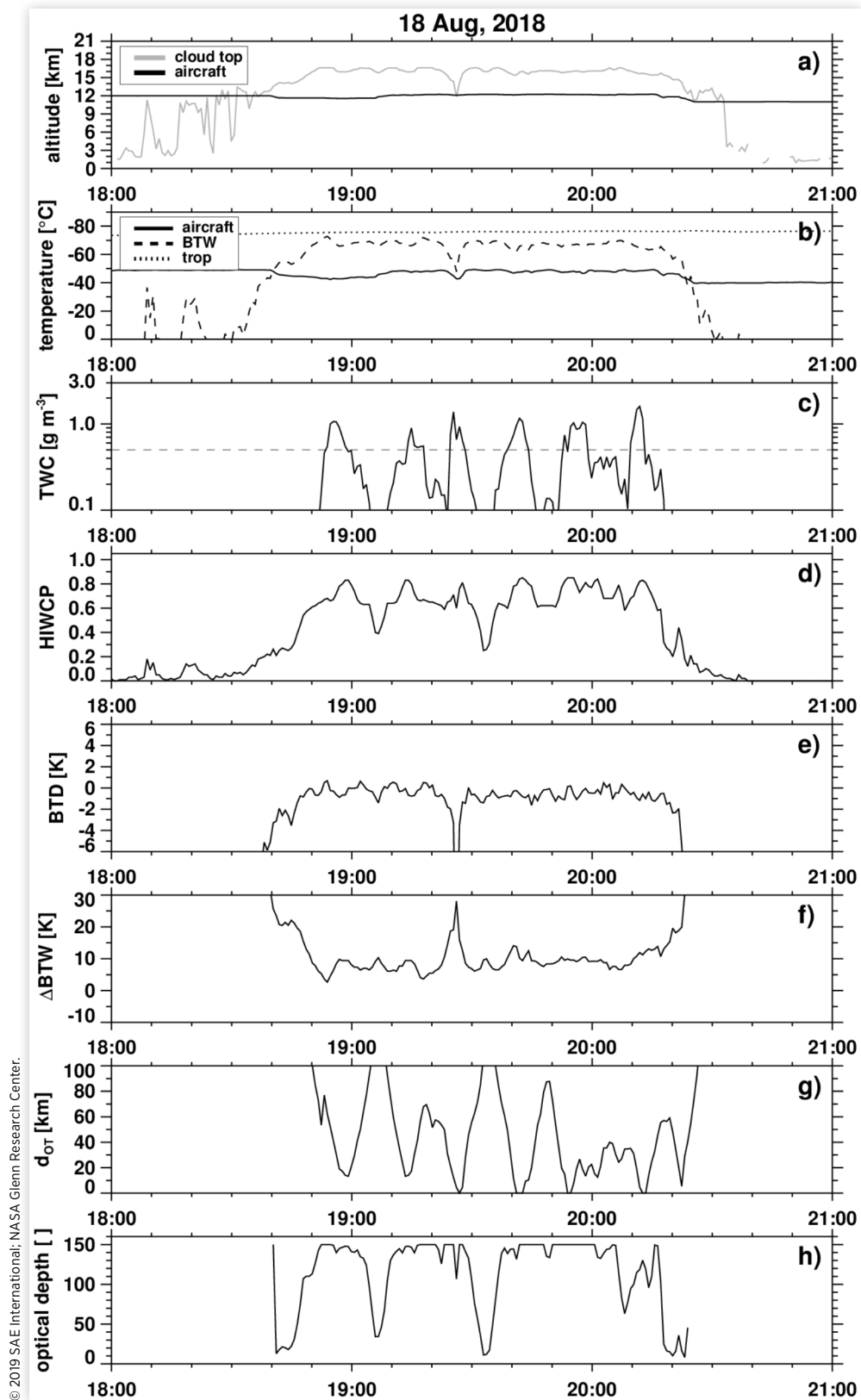
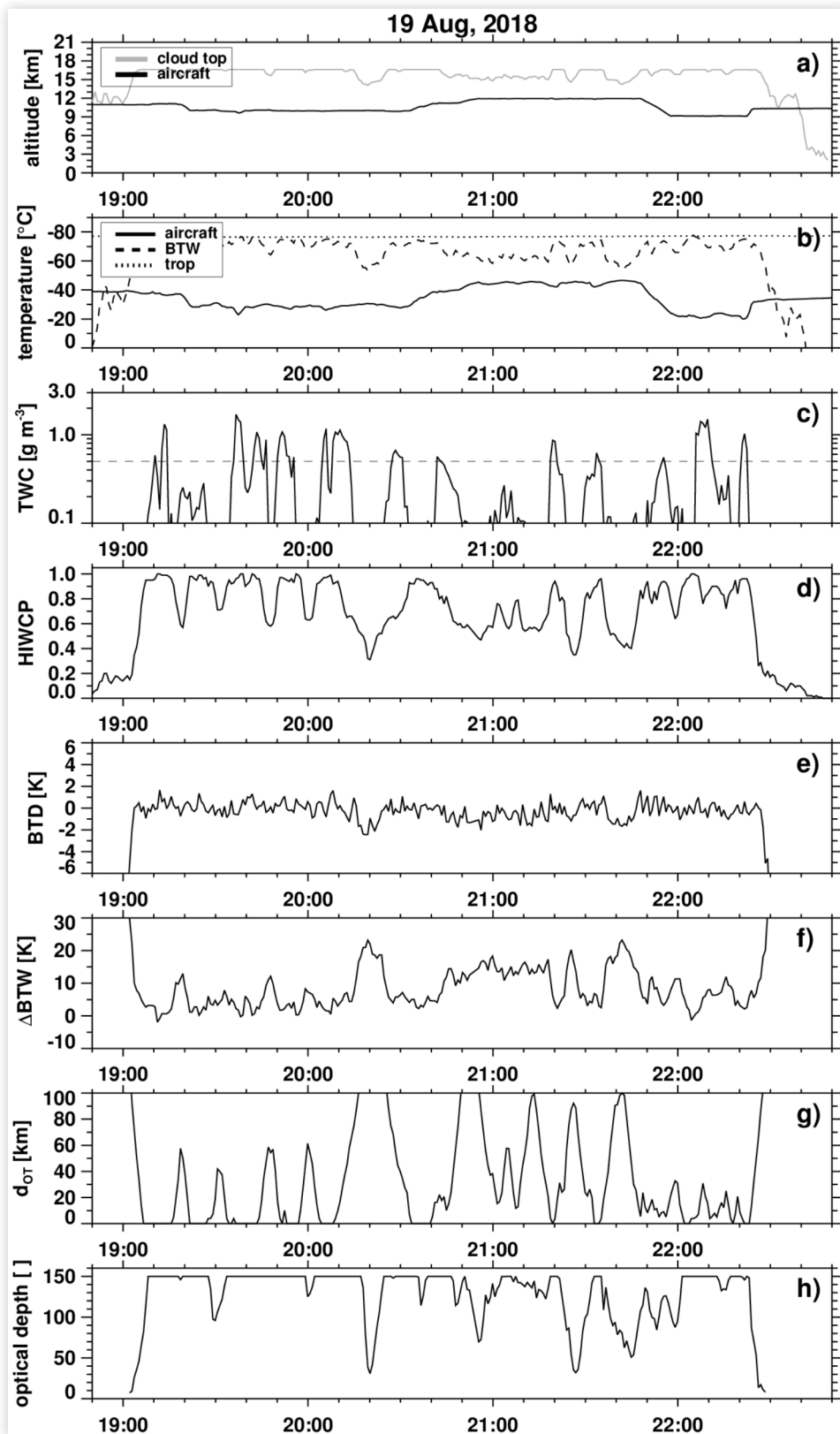
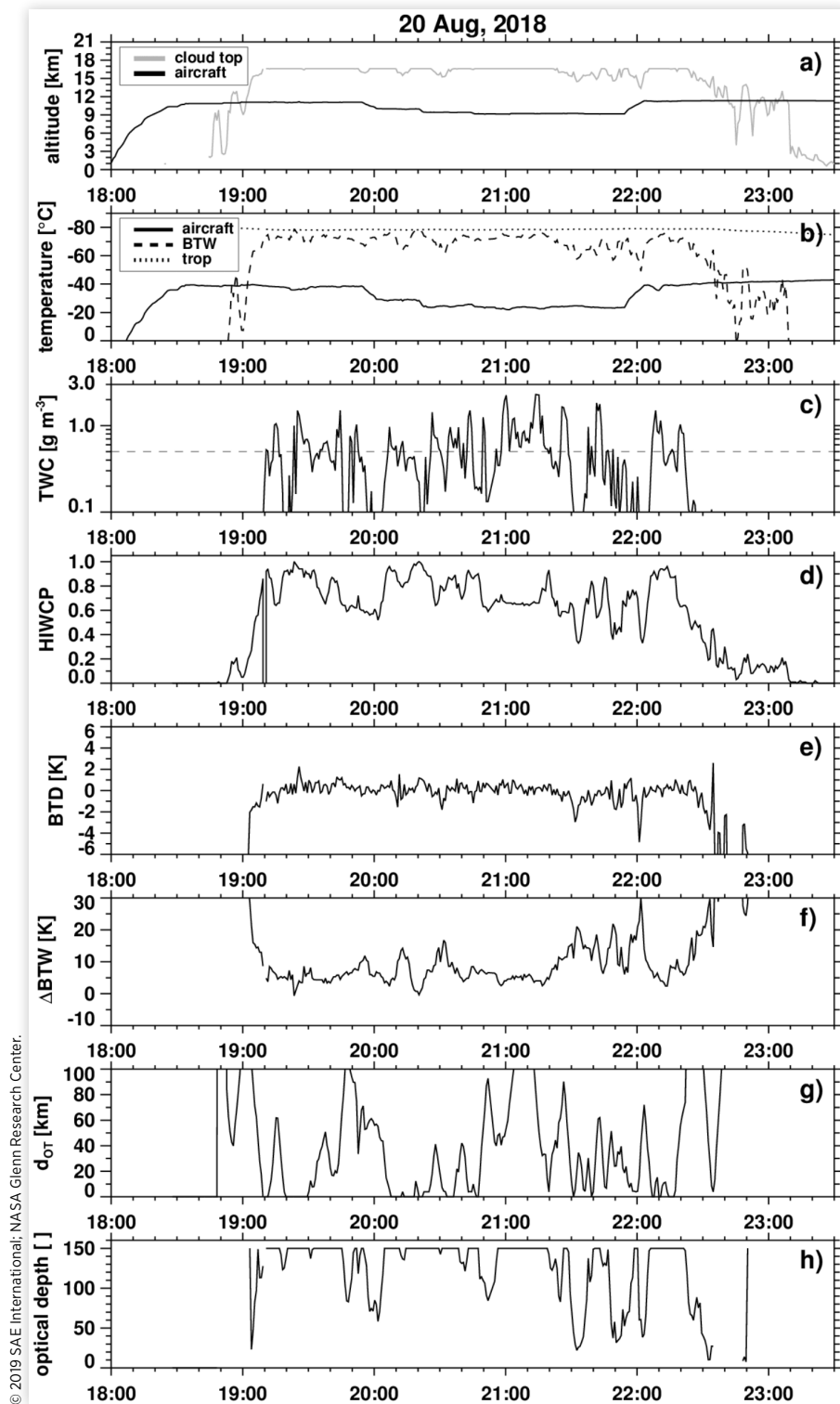


FIGURE 24 Same as Figure 22 but for GOES-15 data on 19 August 2018. The GOES-15 Imager observed these storms with an irregular scan pattern as described in the text above.



© 2019 SAE International; NASA Glenn Research Center.

FIGURE 25 Same as Figure 22 but for GOES-15 data on 20 August 2018. The GOES-15 Imager observed these storms at 30-minute intervals, at approximately 10 and 40 minutes after the hour.



© 2019 SAE International; NASA Glenn Research Center. This is the work of a Government and is not subject to copyright protection. Foreign copyrights may apply. The Government under which this work was written assumes no liability or responsibility for the contents of this work or the use of this work, nor is it endorsing any manufacturers, products, or services cited herein and any trade name that may appear in the work has been included only because it has been deemed essential to the contents of the work.

Positions and opinions advanced in this work are those of the author(s) and not necessarily those of SAE International. Responsibility for the content of the work lies solely with the author(s).